

**Best Available
Copy
for all Pictures**

AD/A-001 971

OPTICS RESEARCH: 1974:1

Robert H. Rediker

Massachusetts Institute of Technology

Prepared for:

Electronic Systems Division
Advanced Research Projects Agency

30 June 1974

DISTRIBUTED BY:

NTIS

National Technical Information Service
U. S. DEPARTMENT OF COMMERCE

The work reported in this document was performed at Lincoln Laboratory, a center for research operated by Massachusetts Institute of Technology. This work was sponsored in part by the Advanced Research Projects Agency of the Department of Defense (ARPA Order 600) and in part by the Department of the Air Force under Contract F19628-73-C-0002. Where noted, research sponsored by the Environmental Protection Agency and National Science Foundation is included.

This report may be reproduced to satisfy needs of U.S. Government agencies.

This technical report has been reviewed and is approved for publication.

FOR THE COMMANDER

Eugene C. Raabe
Eugene C. Raabe, Lt. Col., USAF
Chief, ESD Lincoln Laboratory Project Office

ACCESSION for	
NTIS	White Section <input checked="" type="checkbox"/>
DTIC	U.S. Section <input type="checkbox"/>
UNCLASSIFIED	<input type="checkbox"/>
BY	
DISTRIBUTION/AVAILABILITY CODES	
Dist.	AVAIL. and/or SPECIAL
A	

Non-Lincoln Recipients
PLEASE DO NOT RETURN
Permission is given to destroy this document
when it is no longer needed.

ia

UNCLASSIFIED

SECURITY CLASSIFICATION OF THIS PAGE (When Data Entered)

REPORT DOCUMENTATION PAGE		READ INSTRUCTIONS BEFORE COMPLETING FORM
1. REPORT NUMBER ESD-TR-74-235	2. GOVT ACCESSION NO.	3. RECIPIENT'S CATALOG NUMBER AD/A-001971
4. TITLE (and Subtitle) OPTICS RESEARCH		5. TYPE OF REPORT & PERIOD COVERED Semiannual Report 1 January through 30 June 1974
		6. PERFORMING ORG. REPORT NUMBER Optics Research (1974:1)
7. AUTHOR(s) Robert H. Rediker		8. CONTRACT OR GRANT NUMBER(s) F19628-73-C-0002
9. PERFORMING ORGANIZATION NAME AND ADDRESS Lincoln Laboratory, M.I.T. P.O. Box 73 Lexington, MA 02173		10. PROGRAM ELEMENT, PROJECT, TASK AREA & WORK UNIT NUMBERS ARPA Order 600
11. CONTROLLING OFFICE NAME AND ADDRESS Advanced Research Projects Agency 1400 Wilson Blvd Arlington, VA 22209		12. REPORT DATE 30 June 1974
14. MONITORING AGENCY NAME & ADDRESS (if different from Controlling Office) Electronics Systems Division Hanscom AFB Bedford, MA 01730		13. NUMBER OF PAGES 53
		15. SECURITY CLASS. (of this report) Unclassified
		15a. DECLASSIFICATION DOWNGRADING SCHEDULE
16. DISTRIBUTION STATEMENT (of this Report) Approved for public release; distribution unlimited.		
17. DISTRIBUTION STATEMENT (of the abstract entered in Block 20, if different from Report)		
18. SUPPLEMENTARY NOTES None		
<div style="text-align: right;"> Reproduced by NATIONAL TECHNICAL INFORMATION SERVICE US Department of Commerce Springfield, VA. 22151 </div>		
19. KEY WORDS (Continue on reverse side if necessary and identify by block number)		
<div style="display: flex; justify-content: space-between;"> <div> optics laser technology thermal blooming </div> <div> optical devices optical systems </div> <div> KC-135 laser radar imaging system </div> </div>		
20. ABSTRACT (Continue on reverse side if necessary and identify by block number)		
<p>This report covers work of the Optics Division at Lincoln Laboratory for the period 1 January through 30 June 1974. The topics covered are laser technology and propagation and optical measurements and instrumentation.</p> <p>Additional information on the optics program may be found in the semiannual technical summary reports to the Advanced Research Projects Agency.</p>		

DD FORM 1473 EDITION OF 1 NOV 65 IS OBSOLETE

★U.S. GOVERNMENT PRINTING OFFICE: 1974 600-028/99

UNCLASSIFIED

SECURITY CLASSIFICATION OF THIS PAGE (When Data Entered)

1

1974

Issued 7 November 1974

Optics Research

Prepared for the Advanced Research Projects Agency
and the Department of the Air Force
under Electronic Systems Division Contract F19628-73-C-0002 by

Lincoln Laboratory

MASSACHUSETTS INSTITUTE OF TECHNOLOGY

LEXINGTON, MASSACHUSETTS



ABSTRACT

This report covers work of the Optics Division at Lincoln Laboratory for the period 1 January through 30 June 1974. The topics covered are laser technology and propagation and optical measurements and instrumentation.

Additional information on the optics program may be found in the semiannual technical summary reports to the Advanced Research Projects Agency.

CONTENTS

Abstract	iii
Introduction	vii
Reports on Optics Research	ix
Organization	xii
 I. LASER TECHNOLOGY AND PROPAGATION	 1
A. Pulse Propagation	1
1. Theory	1
2. Double-Pulse Propagation Experiment	7
B. Effects	9
1. Double-Pulse Impulse Experiments	9
2. Laser-Generated Electron Distribution in Front of Target	12
3. Fast Thermocoupling of Targets	15
C. Devices	15
1. H ₂ -HF Laser	15
2. Long-Pulse HF Chemical Laser	19
3. Electron-Beam-Initiated HF Laser	20
4. HF Electric Discharge Laser	21
5. Progress in CO ₂ Isotope Lasers	21
 II. OPTICAL MEASUREMENTS AND INSTRUMENTATION	 25
A. Interferometric Image Evaluation	25
1. 10.6- μ m MTF Measurement	25
2. Visible Region, 600-Meter-Range MTF Measurements	27
3. Long-Path (Star-Source) Atmospheric MTF Measurements	27
4. Wind-Tunnel MTF Measurements	31
5. Conclusion	36
B. Long-Path Monitoring of Atmospheric Carbon Monoxide by a Tunable Diode Laser System	37

INTRODUCTION

I. LASER TECHNOLOGY AND PROPAGATION

An analysis of the effects of aerosol particle heating on laser beam propagation has been carried out. The thermal blooming due to aerosol heating is shown to be identical to molecular blooming and is characterized by the particle absorption coefficient α_a . The Rayleigh-Gans scattering coefficient from the index spheres is also calculated.

A mathematical expression is derived for the autocorrelation function of the phase change due to an ensemble of aerosol particles which is subjected to irradiation by a laser beam of finite width.

Initial experimental results have been obtained on double-pulse thermal blooming effects which simulate the first two pulses of a slewed repetitively pulsed laser. The results are compared with theoretical predictions and show qualitatively good agreement.

Measurements of specific focal spot impulse delivered to an aluminum target by two CO_2 laser pulses in air are reported, and delay times for recovery of specific impulse to single-pulse values were observed to be about 30 msec for the case of no crossflow of air over the target.

The electron density distribution generated by a 10.6- μm laser pulse focused to 10^6 W/cm^2 on an aluminum target was measured interferometrically.

An experimental program has been initiated to measure the heating of metallic surfaces due to irradiation with 10.6- μm laser radiation in both the presence and absence of plasma formation at the target surface. Preliminary surface temperature measurements have been made with a copper target and fast thin-film thermocouples.

The technique of direct electrical excitation of a H_2 -HF gas mixture in order to obtain high-power, long-pulse HF laser oscillation has been tried and found to be successful. Unoptimized pulsed energy densities of 1.5 joules/liter were obtained with pulse lengths variable from 1 to 4 μsec .

An electron-beam-initiated long-pulse HF laser has been built and tested. Its maximum pulse energies and widths to date have been 1 joule and 3 μsec , respectively.

Construction of an electron-beam-initiated HF laser was completed. Twenty-joule pulses of 200-nsec duration were obtained.

The HF electric discharge laser was scaled up in both physical size and energy input. Energy output was increased from 2.25 to 6.0 joules.

Microwave frequency counter measurements of difference frequencies between stabilized $^{16}\text{O}^{12}\text{C}^{18}\text{O}$ isotope and $^{12}\text{C}^{16}\text{O}_2$ reference lasers were used to calculate the band centers and rotational constants of $^{16}\text{O}^{12}\text{C}^{18}\text{O}$ to within a few kHz. Numerous $^{16}\text{O}^{13}\text{C}^{18}\text{O}$ laser transitions have also been observed.

II. OPTICAL MEASUREMENTS AND INSTRUMENTATION

The laboratory fast-shearing interferometer (FSI) was converted into an infrared operating unit, and a test to check its operation at $10.6\text{ }\mu\text{m}$ with a CO_2 laser was carried out. In addition, a new engineered fast-shearing interferometer has been used in several field experiments to carry out MTF measurements.

The engineered visible FSI was tested over a 600-m range with a laser source, and a star source was observed from the ground, to obtain preliminary MTF data along a variety of atmospheric propagation paths. The interferometer has also been flown on the NASA AMES C-141 airplane, fitted to the 91.5-cm airborne telescope, and some star tests carried out to obtain flight MTF data.

In addition, several different wind tunnels have been investigated with the objective of determining which one or type might be the cleanest optically for future optical propagation experiments.

These short preliminary experiments have resulted in the collection of a large amount of MTF data (over one million MTF curves) in a very short period of time. A detailed analysis of the data has yet to be carried out, and will require a considerable amount of time and effort. A brief outline of the results being obtained with the interferometer is reported here in order to demonstrate its performance in a variety of field environments and to provide a "quick-look" assessment of different atmospheric propagation conditions.

Long-path ambient monitorings of carbon monoxide have been accomplished with a tunable $\text{PbS}_{1-x}\text{Se}_x$ ($x = 0.185$) diode laser system. The laser was operated in a commercially available closed-cycle cryogenic cooler instead of the conventional liquid-helium dewar. Field measurements of the CO levels were taken by tuning the laser for resonant absorption spectroscopy at a fundamental CO vibrational mode in the frequency region of 2110 cm^{-1} . The present system was found to have a minimum detectable signal for CO of ± 2.5 parts per billion (ppb) over the 610-meter path. A similar system is being installed inside a mobile van for participation in the first Regional Air Pollution studies by the U. S. Environmental Protection Agency in St. Louis, Missouri.

REPORTS ON OPTICS RESEARCH

1 January through 30 June 1974

PUBLISHED REPORTS

Journal Articles

JA No.

4147	Aerosol Clearing with a 10.6- μ m Precursor Pulse	D. E. Lencioni J. E. Lowder	IEEE J. Quantum Electron. <u>QE-10</u> , 235-238 (February 1974)
4198	Beam Diagnostics for High Energy Pulsed CO ₂ Lasers	R. W. O'Neil H. Kleiman L. C. Marquet C. W. Kilcline D. Northam*	Appl. Opt. <u>13</u> , 314-321 (February 1974)
4200	The Observation of Diffusion as an Effective Vibrational Relaxation Rate in CO ₂	H. Granek	IEEE J. Quantum Electron. <u>QE-10</u> , 320-325 (March 1974)
4210	Determination of Laser Line Frequencies and Vibrational-Rotational Constants of the ¹² C ¹⁸ O ₂ , ¹³ C ¹⁶ O ₂ , and ¹³ C ¹⁸ O ₂ Isotopes from Measurements of CW Beat Frequencies with Fast HgCdTe Photodiodes and Microwave Frequency Counters	C. Freed A. H. M. Ross* R. G. O'Donnell	J. Mol. Spectrosc. <u>49</u> , 439-453 (1974)
4218	Phase Compensation for Thermal Blooming	L. C. Bradley J. Herrmann	Appl. Opt. <u>13</u> , 331-334 (February 1974)
4239	Measurement of CO ₂ -Laser-Generated Impulse and Pressure	J. E. Lowder L. C. Pettingill	Appl. Phys. Lett., <u>24</u> 204-207 (15 February 1974) DDC AD-778470
4255	High-Energy CO ₂ Laser Pulse Transmission Through Fog	J. E. Lowder H. Kleiman R. W. O'Neil	J. Appl. Phys., <u>45</u> , 221-223 (January 1974)
4258	Large Effective Fresnel Number Confocal Unstable Resonators: an Experimental Study	H. Granek A. J. Morency	Appl. Opt. <u>13</u> , 368-373 (February 1974)
4292	Observation of Hydrodynamic Effects on Thermal Blooming	R. W. O'Neil H. Kleiman J. E. Lowder	Appl. Phys. Lett., <u>24</u> 118-120 (1 February 1974) DDC AD-777558/8

* Author not at Lincoln Laboratory.

JA No.

- | | | | |
|------|--|---------------------------|---|
| 4317 | Spatial Distribution of Electrons in a High-Pressure Plasma Produced by Two-Step Photoionization | J. S. Levine
A. Javan* | Appl. Phys. Lett., <u>24</u> , 258-261
(15 March 1974) |
| 4324 | Laser-Induced Air Breakdown for a 1.06- μ m Radiation | D. Lencioni | Appl. Phys. Lett. <u>25</u> , 15-17
(1 July 1974) |

Meeting Speech†MS No.

- | | | | |
|------|----------------------------------|---|---|
| 3631 | Precision Heterodyne Calibration | C. Freed
D. L. Spears
R. G. O'Donnell
A. H. M. Ross* | Proceedings of the Laser Spectroscopy Conference, Vail, Colorado, 25-29 June 1973 |
|------|----------------------------------|---|---|

* * * * *

UNPUBLISHED REPORTS

Meeting Speeches†MS No.

- | | | | |
|-------|--|--|--|
| 3671 | Bistatic Monitoring of Gaseous Pollutants with Tunable Semiconductor Lasers | E. D. Hinkley | 1974 Pittsburgh Conference on Analytical Chemistry & Applied Spectroscopy, Cleveland, Ohio, 4-8 March 1974 |
| 3671A | Diode Laser Pollutant Monitoring | E. D. Hinkley | Seminar CM Research Laboratory, Warren, Michigan, 5 March 1974 |
| 3742 | 77° K InSb Isolator for 10.6 μ Using an Optimum Carrier Concentration | W. E. Bicknell
L. R. Tomasetta
D. H. Bates | VIII International Quantum Electronics Conference 1974, San Francisco, California, 10-13 June 1974 |
| 3761 | Rapid, Real-Time MTF Measurements in a Field Environment | D. Kelsall | S.P.I.E. Seminar, Rochester, New York, 20 May 1974 |
| 3810 | Review of the Design and Stability of Stable CO ₂ and CO Lasers: Precision Heterodyne Calibration | C. Freed | Seminar at Los Alamos Scientific Laboratory, 17 April 1974; and Seminar at National Bureau of Standards, 19 April 1974, Boulder, Colorado. |

* Author not at Lincoln Laboratory.

† Titles of Meeting Speeches are listed for information only. No copies are available for distribution.

MS No.

3813 Low-Background LWIR
Vidicon

W. J. Scouler
T. M. Quist
J. Rotstein
J. P. Baukus
J. O. Dimmock

22nd National IRIS Symposium,
Wright-Patterson AFB,
Ohio, 22-23 May 1974

3844 Progress in CO₂
Isotope Lasers

C. Freed
A. H. M. Ross*
R. G. O'Donnell

VIII International Quantum
Electronics Conference 1974,
San Francisco, California,
10-13 June 1974

* Author not at Lincoln Laboratory.

ORGANIZATION

OPTICS DIVISION

R. H. Rediker, *Head*
L. B. Anderson, *Associate Head*
M. J. Hudson, *Assistant*

LASER TECHNOLOGY

S. Edellberg, *Leader*
L. C. Marquet, *Associate Leader*

Ariel, E. D.
Bradley, L. C.
Braman, C. E.
Brennan, M. J.
Bushee, J. F., Jr.
Dickey, D. H.
Ferdinand, A. P., Jr.
Finne, P. C.
Fouche, D. G.
Granek, H.
Herrmann, J.

Johnson, J. Q.
Kafalas, P.
Kilcline, G. W.
Kleiman, H.
Kramer, R.
Lencioni, D. E.
Levine, J. S.
Lowder, J. E.
Marcus, S.
Morency, A. J.
O'Neil, R. W.

Osgood, R. M.
Pettingill, L. C.
Pike, H. A.
Pirroni, J. S.
Pitts, R. F.
Scott, W. L., Jr.
Shey, S. Y.
Stiehl, W. A.
Theriault, J. R.
Vernon, H. M., Jr.

ADVANCED SENSORS

J. O. Dimmock, *Leader*
E. S. Cotton, *Associate Leader*
T. M. Quist, *Assistant Leader*

Baukus, J. P.
Bielinski, J. R.
Bollman, R. A.
Chaulk, L. W.
Corbosiero, D. M.
Ellis, R. H.
Hinkley, E. D.
Kelsall, D.

Keyes, R. J.
Ku, R. T.
Marshall, A. P.
McPherson, R. D.
Mudgett, D. A.
Nork, L. P.
Page, D. A.
Perry, F. H.

Rotstein, J.
Sample, J. O.
Scouler, W. J.
Sullivan, F. M.
Swedberg, J. L.
Thomas, M. A.
Weaver, L. D.
Zwicker, H. R.

OPTO-RADAR SYSTEMS

A. B. Gschwendtner, *Leader*
P. R. Longaker, *Assistant Leader*

Bauer, J. R.
Billups, R. R.
Brownson, J. S.
Clay, W. G.
Coles, R. M.
Cordova, R. J.

DiMarzio, E. W.
Dyjak, C. P.
Edwards, D. M.
Hull, R. J.
Johns, T. W.

McPhie, J. M.
Merrill, E. R.
Rosato, N. F.
Stevens, R. R.
Zieman, H. E.

LASER SYSTEMS

R. H. Kingston, *Leader*
L. J. Sullivan, *Associate Leader*
P. A. Ingwersen, *Assistant Leader*

Bates, D. H.
Bicknell, W. E.
Capes, R. N., Jr.
Daley, J. A., Jr.
Fiasconaro, J. G.
Freed, C.

Fulton, M. J.
Gilmartin, T. J.
Holtz, J. Z.
Malling, L. R.
Marapoti, J. V.
O'Donnell, R. G.

Parker, A. C.
Swezey, L. W.
Teoste, R.
Valcourt, G. I.
Ziegler, H. L.
Zimmerman, M. D.

1. LASER TECHNOLOGY AND PROPAGATION

A. PULSE PROPAGATION

1. Theory

a. Effects of Aerosol Particle Heating on Laser Beam Propagation

An analysis has been carried out for the heating of atmospheric particulates due to absorption of laser beam energy with conduction to the surrounding air. The effects of the hot air spheres on beam propagation were evaluated by considering the scattering from the spheres and the thermal blooming due to the gross phase change of rays passing through many index spheres. The details of the calculation will appear in Project Report LTP 27 (Ref. 1). A few of the main results are given below.

The equilibrium temperature of a spherical particle of radius a is

$$T_a = T_o [1 + I\sigma_a/2\pi K_o a T_o]^{1/2}$$

where we have assumed a temperature-dependent conductivity.

The characteristic equilibrium time for the particles is

$$\tau = (T_a - T_o) \frac{4\pi a^3 C_s \rho_s}{3I\sigma_a}$$

where

I = laser beam intensity

σ_a = particle absorption cross section

K_o = thermal conductivity of air at ambient temperature T_o

C_s = specific heat of the particle

ρ_s = mass density of the particle

Figures 1-1 and -2 show values for T_a and τ for carbon.

The scattering of radiation from the hot spheres was found to satisfy the condition for Rayleigh-Gans scattering theory which gave a volume scattering coefficient

$$\alpha_{RG} = \frac{9\pi \Delta_o^2 N_o I^2 D t}{2\lambda^2 K_o^2 T_o^2} \int_{a_1}^{a_2} \frac{\sigma_a^2 a^{-4} da}{[1 + \sqrt{t_a/t}]^2}$$

where

$$t_a = \frac{1}{D} \left[\frac{3I\sigma_a}{4\pi K_o T_o} \right]^2$$

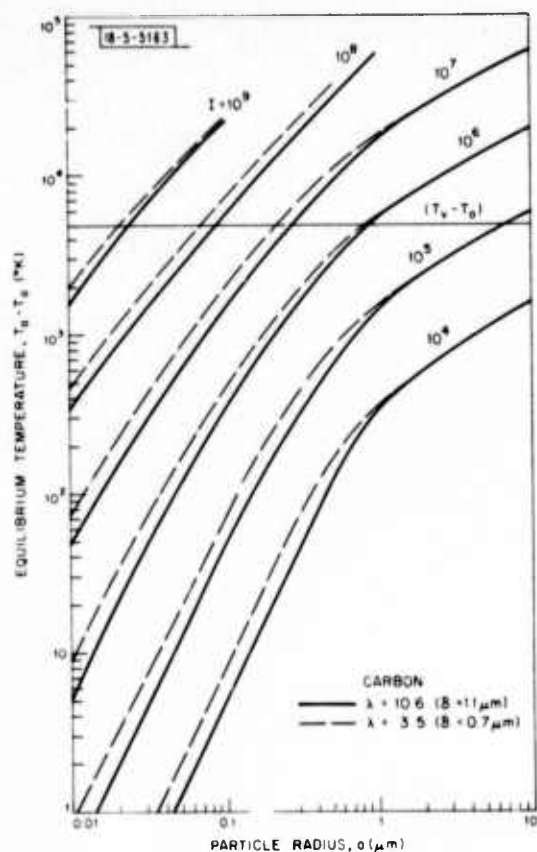
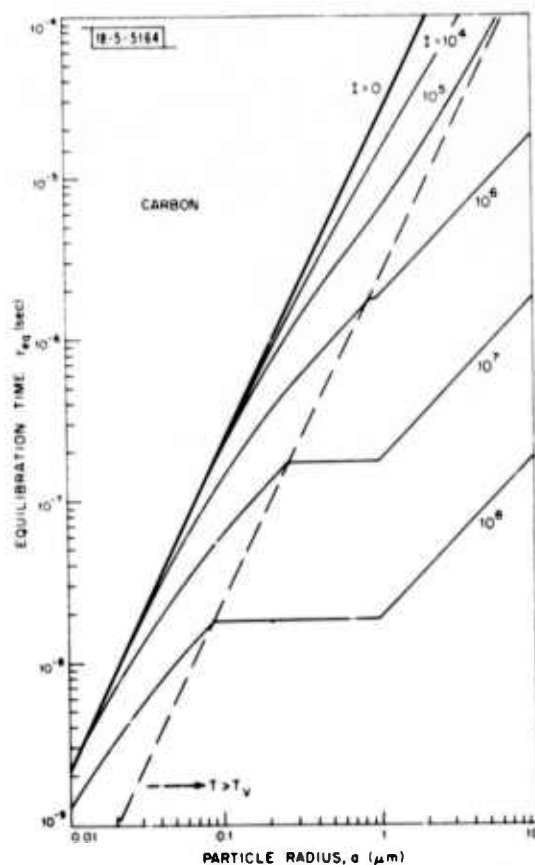


Fig. 1-1. Calculated equilibrium temperature for carbon particles as a function of radius for various laser intensities.

Fig. 1-2. Equilibration time for carbon particles as a function of radius for various laser intensities. The slanted dashed line separates the regions where the final particle temperatures are less or greater than the vaporization temperature.



and

$\Delta_o + 1$ = index of refraction of air

N_o = the coefficient in the aerosol size distribution

D = thermal diffusion coefficient of air

and

λ = laser wavelength

An example of this scattering coefficient for a carbon aerosol is shown in Fig. I-3.

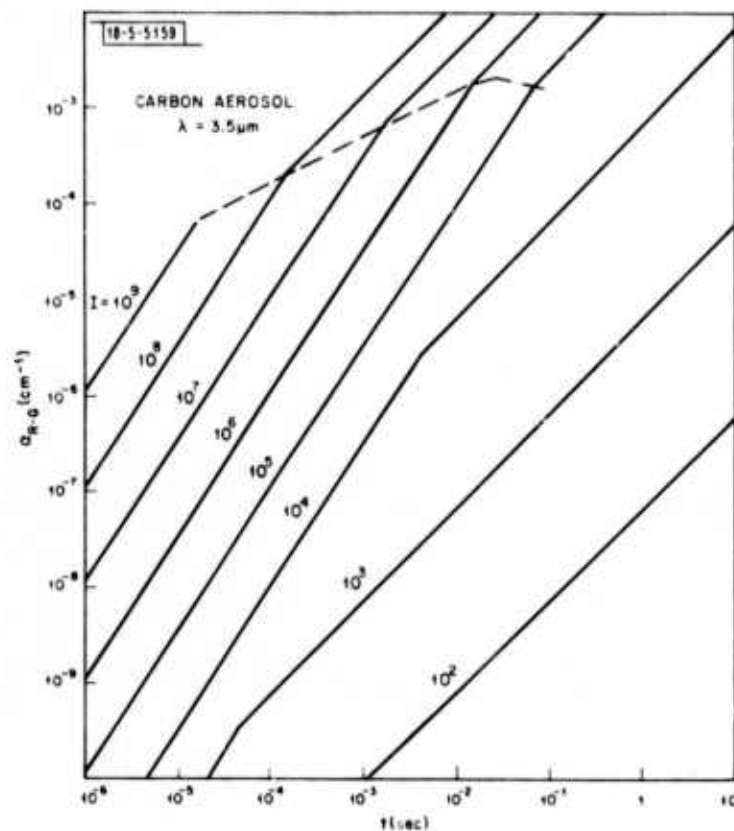


Fig. I-3. The Rayleigh-Gans scattering coefficient for the index spheres around a carbon aerosol as a function of time and for various laser intensities.

The average phase change of a ray at time t in passing through many spheres a distance Δz is

$$\varphi = \frac{\Delta Z k \Delta_o \alpha_a}{\rho_o C_o T_o} \left[\left(\epsilon (t/t_H) - 1 \right) t + \frac{C^2 t^3 \nabla^2}{6} \right]$$

where

k = the wave number

α_a = the aerosol absorption coefficient

ρ_0 = density of air

C_0 = specific heat of air

and

$\epsilon(t/t_H)$ is a function which has the value t for

$t \ll t_H$ and 0 for $t \geq t_H$.

This phase change indicates that the thermal blooming due to aerosol heating is identical to molecular blooming in both the t^3 and t regimes and is characterized by the particle absorption coefficient α_a .

D. E. Lencioni
H. Kleiman

b. Statistics of Phase Distortions Produced by Laser-Heated Aerosols

When we consider the propagation of a laser beam through an aerosol-laden (or fog-laden) atmosphere, the problem separates into two parts: (1) the effect of the beam on heating the particles and producing an index "sphere" that expands around each particle, and (2) the distortion that the index spheres produce on the propagating radiation. The first part determines the time evolution and magnitude of phase change contributed by each particle and is derived from the physics of particle heating, evaporation, or explosion - whichever is the pertinent regime.

This phase of the problem is being considered by others and will be treated by us separately. In this report we wish to document the mathematics on development of the autocorrelation function of the phase change of the individual particles. Contained in this derivation will be the functions $a(t)$ (vapor sphere radius) and Δn , whose values are determined by part (1).

For a calculation of beam distortion during propagation through an ensemble of index spheres, we need to determine the average phase change due to an index sphere (or the ensemble) and the positional autocorrelation function of the ensemble of spheres.

If we have a uniform index sphere (and ignore the obstruction of the particle at the center since this simply acts as an absorber and, in general, is small compared to the index sphere size) whose phase change per unit length through it is $k_0 \Delta n$, then the phase change of a "ray" passing through at a distance r from the center of the sphere is $2k_0 \Delta n \sqrt{a^2 - r^2}$. For future reference we define the Fourier transform, $v(k)$, of this phase change

$$\int v(k) e^{i\vec{k} \cdot \vec{r}} d^2k = k_0 \int n dz = 2k_0 \Delta n \sqrt{a^2 - r^2} \quad r \leq a \quad (1-1)$$

in the plane transverse to the propagation direction. Then,

$$\begin{aligned} v(k) &= \frac{1}{(2\pi)^2} \int e^{i\vec{k} \cdot \vec{r}} (2k_0 \Delta n \sqrt{a^2 - r^2}) r dr d\varphi \\ &= \frac{\Delta n a^3 k_0}{\pi} \frac{j_1(ka)}{ka} \cong k_0 \frac{\Delta n a^3}{3\pi} \end{aligned} \quad (1-2)$$

where $j_1(ka)$ is the spherical Bessel's function and the last expression is the leading term of the expansion in k . In the December 1973 Optics Research Report it is shown that to first order this spectrum agrees with the spectrum calculated from the scattered wave, so using the geometric optics approximation is appropriate.

We can now find that the average phase change contribution of an ensemble of particles randomly distributed over a path length L is determined by taking the product of the number of encounters per unit beam area and the contribution per encounter to find

$$\langle k_0 \int ndz \rangle = (\pi a^2 L N_0) (4/3 a \Delta n) \quad (1-3)$$

where the last term is determined by averaging the phase change over the index sphere cross section

$$\frac{2\pi \Delta n \int_0^a r^2 \sqrt{a^2 - r^2} dr}{2\pi \int_0^a r dr} = 4/3 a \Delta n \quad (1-4)$$

One can equivalently add the Fourier transform contributions in phase space and perform the inverse transform:

$$\begin{aligned} \langle k_0 \int ndz \rangle &= \int_{z_0}^{z_0+L} N_0 \int_0^\infty dr_j r_j \int_0^\infty dk k J_0(kr) J_0(kr_j) \left(\frac{a^3 \Delta n}{3\pi} \right) \\ &= \int_{z_0}^{z_0+L} N_0 \int_0^\infty dr_j r_j \frac{(2\pi)^2}{r_j} \delta(r - r_j) \left(\frac{a^3 \Delta n}{3\pi} \right) \\ &= N_0 L \frac{4}{3} a^3 \Delta n \pi \\ &= N_0 L V_s \Delta n \end{aligned} \quad (1-5)$$

where $V_s = 4/3 \pi a^3$ is the index sphere volume. Or finally one can use the probability distribution that we shall next derive (in determination of the autocorrelation function) to arrive at the same answer for the average phase change due to the ensemble.

We ask now what is the probability

$$P_\xi(n, x_1 < x < x_2, y_1 < y < y_2, z_1 < z < z_2)$$

that the random variable ξ , the number of particles in a given volume, takes on the value n in the particular volume

$$V = \rho_x \rho_y L = (x_2 - x_1) (y_2 - y_1) (z_2 - z_1) \quad .$$

We know from the nature of the model that the mean number of particles in a given volume V is

$$\bar{\xi} = \sum_{n=0}^{\infty} n P_\xi(n, V) = N_0 V \quad (1-6)$$

If we make the assumptions that the number of particles in a given volume element is probabilistically independent of the number in any other volume element and that the probability of more than one particle being in an infinitesimal volume element $dV = d\rho_x d\rho_y L$ is infinitesimally smaller than the probability of one particle being in the same volume, this problem then becomes completely analogous to the case of the one-dimensional Poisson distribution and the desired probability is just

$$P_\xi(n, V) = \frac{(N_0 V)^n}{n!} e^{-N_0 V} \quad (1-7)$$

where $V = \rho_x \rho_y L$. (A convenient source for the development of the Poisson distribution is presented on pp. 177-186 in Statistical Theory of Communication, by Y.W. Lee, where the substitution of N_0 for k and $\rho_x \rho_y L = V$ for τ should be made for our case.)

We now ask what is the autocorrelation function of the phase changes due to the index spheres of these randomly distributed particles. Since the extent of the index spheres, and certainly of the particles themselves, is small compared to the dimensions of the beam and propagation distances, one can consider the spheres to be delta functions in space for averaging over position if one properly takes into account the magnitude of phase change contributed by each particle. The corresponding autocorrelation function for two positions separated by a distance r is then

$$\begin{aligned} \psi(r) &= (V_s \Delta n)^2 \sum_{j=-\infty}^{\infty} \sum_{i=-\infty}^{\infty} x_{1i} x_{2j} P_{\xi_1 \xi_2}(x_{1i}, x_{2j}; V) \\ &= (V_s \Delta n)^2 \sum_{j=-\infty}^{\infty} \sum_{i=-\infty}^{\infty} x_{1i} x_{2j} P_{\xi_1}(x_{1i}) P_{\xi_2, \xi_1}(x_{2i} | x_{1i}; V) \end{aligned} \quad (1-8)$$

We define the two-dimensional unit impulse function in the limiting sense; namely, it is a pulse of constant height A and extent $d\rho_x d\rho_y$, such that the area is a constant of unity as $d\rho_x d\rho_y$ becomes vanishingly small:

$$A d\rho_x d\rho_y \Big|_{\substack{A \rightarrow \infty \\ d\rho_x d\rho_y \rightarrow 0}} = 1 \quad (1-9)$$

If we pick a given position, the probability of a particle being in the differential volume element and thus yielding an amplitude $\xi_1 = A$ is

$$P_{\xi_1}(A) = N_0 d\rho_x d\rho_y L \quad (1-10)$$

and otherwise ξ_1 is zero.

From Eq. (1-8), for $r = 0$, then

$$\begin{aligned} \psi_{pp}(0) &= x_{11}^2 P_{\xi_1}(x_{11}) (V_s \Delta n)^2 \\ &= A^2 N_0 (d\rho_x d\rho_y L) \Big|_{A \rightarrow \infty} (V_s \Delta n)^2 \\ &= N_0 L A \Big|_{A \rightarrow \infty} (V_s \Delta n)^2 \\ &= N_0 L (V_s \Delta n)^2 \delta(x) \Big|_{x=0} \delta(y) \Big|_{y=0} \end{aligned} \quad (1-11)$$

where $\delta(x)$ and $\delta(y)$ are one-dimensional Dirac delta functions. For $r \neq 0$,

$$P_{\xi_2}[\xi_1(x_{2j} | x_{1i}; V)] = P_{\xi_2}(x_{2j}) = P_{\xi_1}(x_{1i}) \quad (1-12)$$

by the assumption of independence of particles occurring in different volume elements. Then by Eq. (1-8),

$$\begin{aligned} \varphi_{pp}(\vec{r}) &= A^2 N_o (d\rho_x d\rho_y L) N_o (d\rho_x d\rho_y L) \Big|_{A \rightarrow \infty} (V_s \Delta n)^2 \\ &= N_o^2 L^2 (V_s \Delta n)^2 \end{aligned} \quad (I-13)$$

The total expression for the autocorrelation function is then from Eqs. (I-11) and (I-13)

$$\varphi_{pp}(\vec{r}) = \{N_o L \delta(x) \delta(y) + N_o^2 L^2 (V_s \Delta n)^2\} \quad (I-14)$$

We recognize the last term as being the square of the mean phase change

$$\langle k_o \int n dz \rangle^2 = \left[V_s \Delta n \sum_{j=0}^1 x_{1j} P_{\xi 1}(x_{1j}) \right]^2 = (V_s \Delta n N_o L)^2 \quad (I-15)$$

Therefore, the autocorrelation function of the fluctuations around the mean is given by

$$\varphi_{pp}(\vec{r}) = N_o L \delta(x) \delta(y) (V_s \Delta n)^2 \quad (I-16)$$

H. Granek

2. Double-Pulse Propagation Experiment

Initial experimental results have been obtained on double-pulse thermal blooming effects which simulate the first two pulses of a slewed repetitively pulsed laser. Figure 1-4 shows the experimental arrangement. Two beams from two CO₂ e-beam pulsed lasers were focused with 48-m optics at a diagnostics table. Side orders from two gratings were used to monitor pulse energy, pulse shape, and beam quality. The two beams were aligned so that they overlapped at the entrance of a 5-m, absorption cell containing a mixture of propane and N₂ at atmospheric pressure. Fast-acting valves at the entrance and exit of the cell were used to contain the absorbing mixture. The energy absorbed from the first pulse through the cell caused a local index

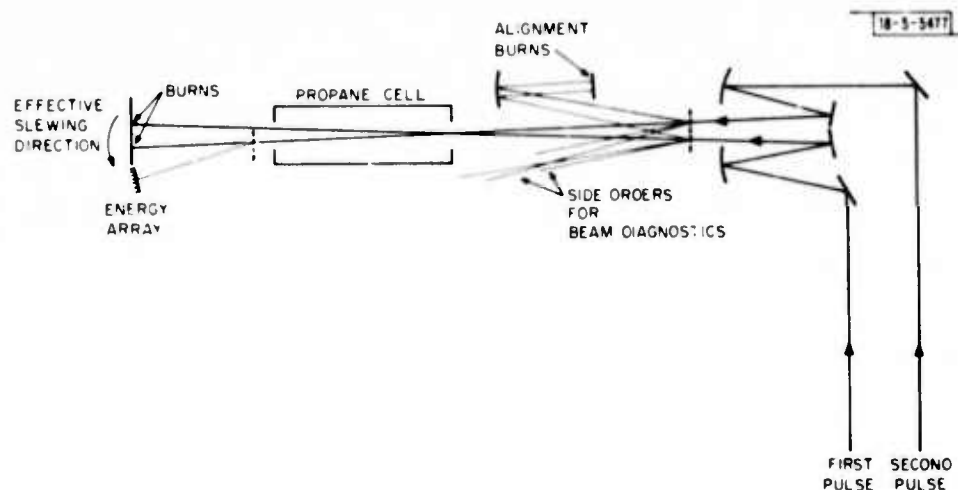


Fig.1-4. Experimental arrangement used in the double-pulse blooming experiment. The beams were focused with 48-m optics at a diagnostic table. The two beams were made to overlap at the entrance to a 5-m absorption cell which simulated a pure slewing within the cell. An order from a grating at the exit to the cell was placed on a 16-element energy array to obtain the one-dimensional energy distribution of the bloomed beam.

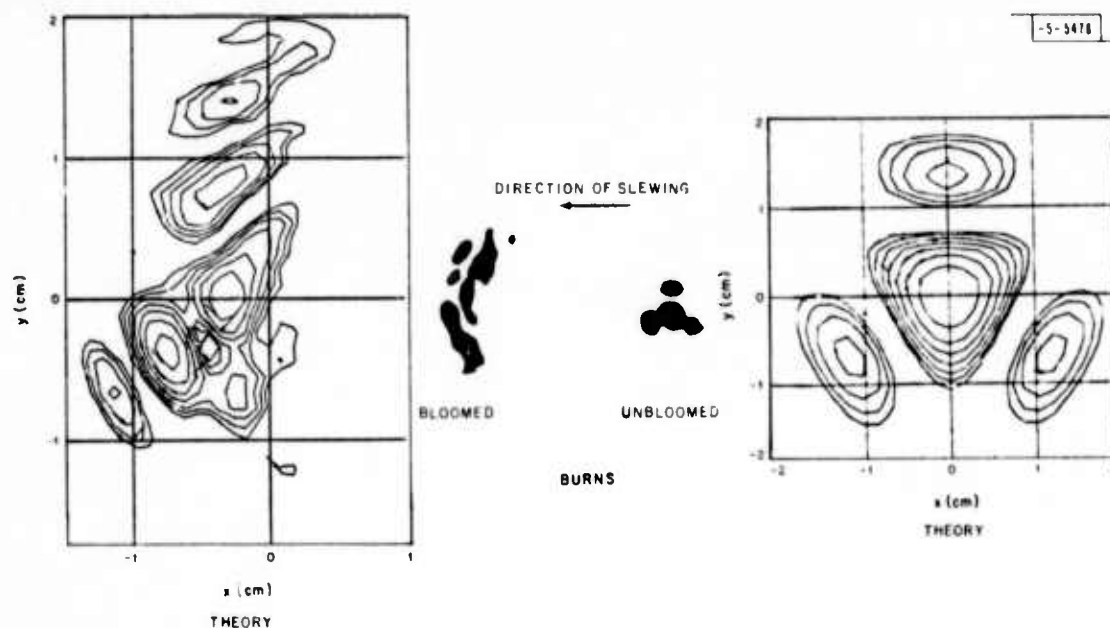


Fig.1-5. Experimental burn patterns of the bloomed and unbloomed pulse are compared to theoretically generated contours under the same conditions. Note the crescent shape of the bloomed beam.

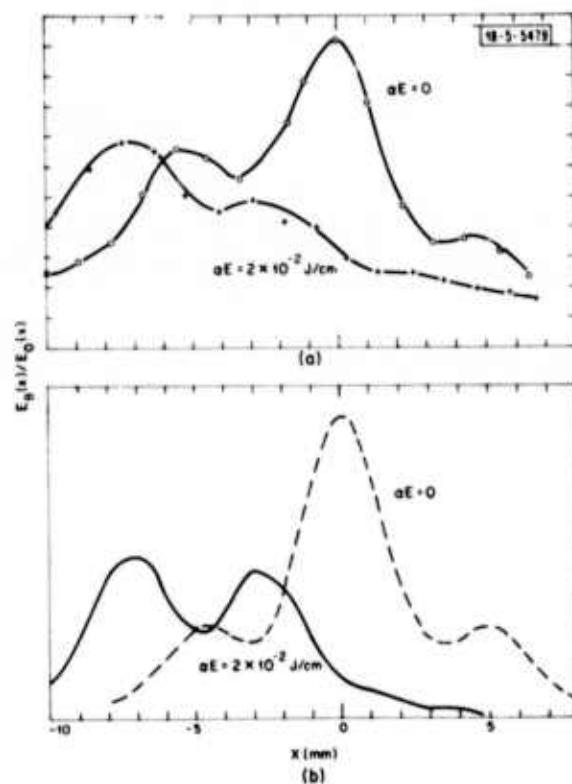


Fig.1-6(a). Experimental one-dimensional energy distributions of a bloomed and unbloomed beam. (b) Theoretically generated distributions with the same absorption conditions. Note the reduction in energy density and the shift of the peak in the direction of slewing.

perturbation. The second pulse which was delayed 10^{-2} sec passed through the cell at a slewed angle relative to the first pulse and resulted in a distortion of the focused beam, the extent of which depended on the absorbed energy of the first pulse. Burn patterns were obtained for the unbloomed first pulse and bloomed second pulse. Figure 1-5 shows a comparison of a bloomed and an unbloomed burn pattern together with theoretically generated contours.

The second pulse passed through a grating after the absorption cell. A side order from this grating was placed on a 16-element linear energy detector array to obtain the one-dimensional distribution of energy in the bloomed beam. Figure 1-6(a) shows energy array measurements for an unbloomed pulse and a bloomed pulse for which $\alpha E_1 = 2 \times 10^{-2}$ J/cm. The bloomed pulse has shifted in the direction of slewing and from Fig. 1-5 the focal pattern is in the form of a crescent. Figure 1-6(b) shows a theoretical comparison of a bloomed and an unbloomed pulse under the same conditions as in the experiment. The fifth-order 120° aberration was introduced into the code calculations in order to approximate the observed focal pattern (see Fig 1-5). The qualitative agreement is good in view of the difficulties of simulating the unbloomed distribution. More detailed measurements are in progress with much better beam quality which should facilitate the data comparison with the computer code results. Also, blooming data are being obtained which simulate slewing plus wind. These data will be reported at a later date.

R. W. O'Neil J. Herrmann
D. E. Lencioni L. Pettingill

B. EFFECTS

1. Double-Pulse Impulse Experiments

Measurements of specific focal spot impulse delivered to an aluminum target by two CO_2 laser pulses in air are reported. The dual 500-J CO_2 laser system was used to provide two coincident high-energy pulses with a variable time delay between them. Delay times for recovery of specific impulse to single-pulse values were observed to be about 30 nsec for the case of no crossflow of air over the target.

The dual CO_2 e-beam laser system described in Ref. 2 has been used to investigate the phenomena of multiple-pulse impulse loading of targets in the atmosphere. The optical arrangement of the system is shown in Fig. 1-7 where M3-1 and M3-2 are 30-m focal length mirrors which are aligned to provide coincident focal spots.

The wire diffraction gratings G1 and G2 were canted at an angle relative to each other so as to separate the diffraction orders of the two laser beams in the focal plane. The individual laser pulse shapes, energies, and focal spot energy densities were determined with photon drag detectors, pyroelectric calorimeters, and thermally sensitive paper placed in the diffraction orders.³

The target for these experiments was a 1/2-inch-thick aluminum plate, in which a sensitive pendulum, which was free to swing in a small hole drilled in the plate, was mounted. The focal spots for the two lasers were aligned on the pendulum which was a 0.38-cm-diameter aluminum rod, and the lasers were fixed with preset delay between the pulses. The pendulum was used to measure the total specific impulse delivered to the target in the area of the focal spot.

The area of the pendulum rod was 0.11 cm^2 which was about 1.5 times the half-power area of the two focal spots. The measured specific impulse is given by

$$I_s (\text{taps}) = \frac{I \text{ dyn} \cdot \text{sec}}{A_t \text{ cm}^2}$$

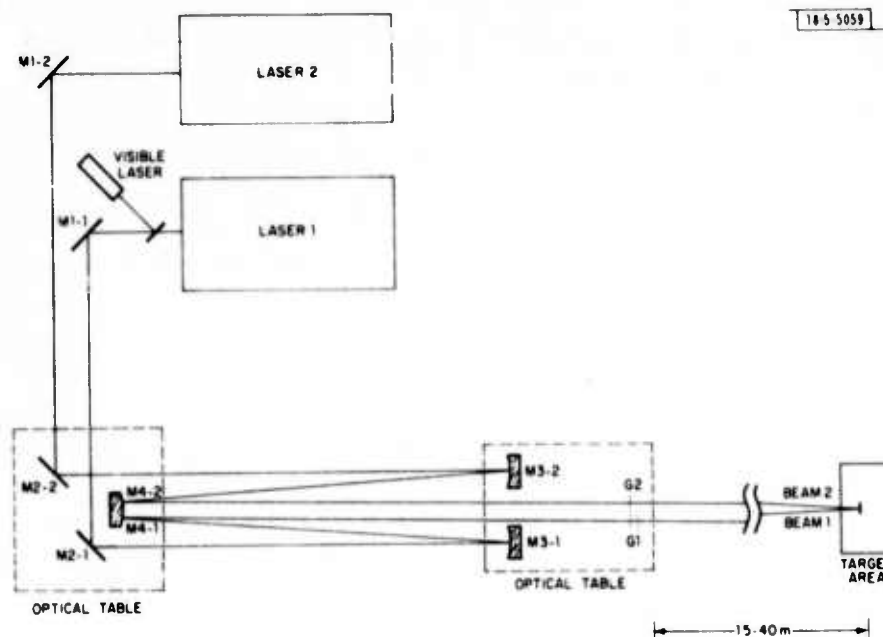


Fig.1-7. Schematic diagram of dual CO₂ laser-optical arrangement.

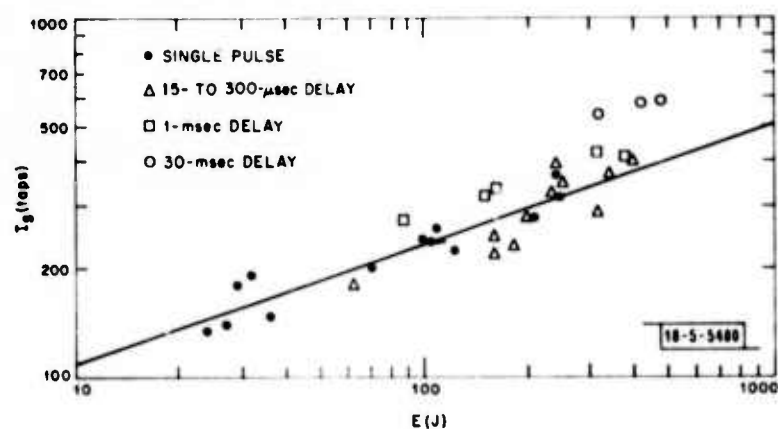


Fig.1-8. Specific impulse delivered to the focal spot as a function to total energy for both single- and double-pulse irradiation.

where l is the total impulse transferred to the pendulum and A_t is the area of the rod. In Fig. 1-8, the measured specific impulse is presented as a function of total energy for both single- and double-pulse shots with various time delays as indicated. The solid line was fit to the single-pulse data (solid symbols) and is given by

$$l_s = 51(E)^{1/3} \quad (1-17)$$

where E is the energy in the pulse. For a fixed pulse length and focal spot size, this relationship is the same as previously noted⁴ where the impulse was proportional to the incident power density to the $1/3$ power. Equation (1-17), then, implies that for two independent pulses, the total impulse is given by

$$l_{s1} + l_{s2} \propto (E_1)^{1/3} + (E_2)^{1/3} \quad (1-18)$$

The double-pulse data for delay times of 15 to 300 μ sec shown in Fig. 1-9 were plotted in the form $l_{s1} + l_{s2} = l_s$ and $E_1 + E_2 = E$. These data indicate that for $\tau_d < 1$ msec the two pulses are not independent, but have the same effect as a single pulse with the same total energy, i.e.,

$$l_s \propto (E_1 + E_2)^{1/3} \quad (1-19)$$

The data for delay times greater than 1 msec show an increased specific impulse for a given total energy and indicate the two pulses are beginning to act independently. To show this effect more clearly the double-pulse impulse data were plotted in normalized form in Fig. 1-9. Here

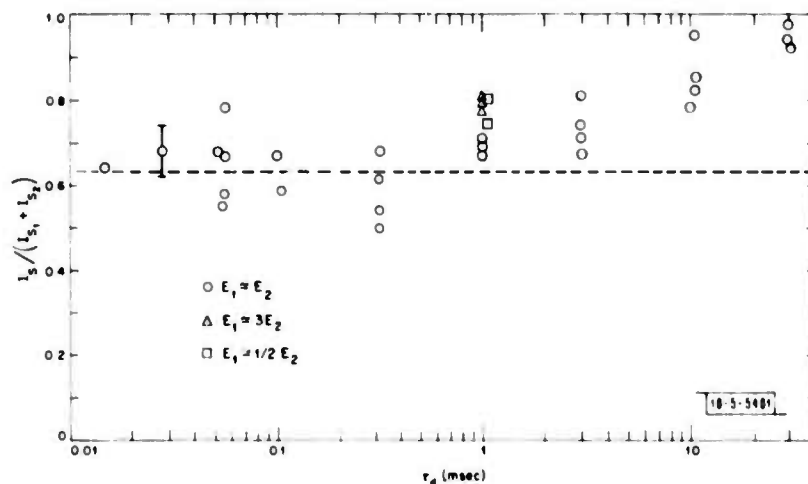


Fig. 1-9. Normalized impulse as a function of delay time between laser pulses. l_s is the measured specific impulse and l_{s1} and l_{s2} are the specific impulses to be expected from single pulses of energies E_1 and E_2 .

l_s is the measured total impulse and l_{s1} and l_{s2} are the specific impulses to be expected from single pulses with energies of E_1 and E_2 . The normalized impulse is plotted as a function of delay time between the two laser pulses. These data show that the impulse "recovery" is not complete for these conditions until after a delay time of about 30 msec. The dashed line in Fig. 1-9 indicates the normalized impulse expected when the two pulses act as a single pulse, i.e., when

$$\frac{I_s}{I_{s_1} + I_{s_2}} = \frac{(E_1 + E_2)^{1/3}}{(E_1)^{1/3} + (E_2)^{1/3}} \quad (1-20)$$

and when $E_1 = E_2$

$$\frac{I_s}{I_{s_1} + I_{s_2}} = \frac{(2)^{1/3}}{2} = 0.63$$

The long delay times necessary for the second pulse to act independently of the first, seem to be due to particulates, which are generated by the first pulse and act as breakdown triggers in the focal volume when irradiated by the second pulse. In Fig. 1-10 typical streak photographs

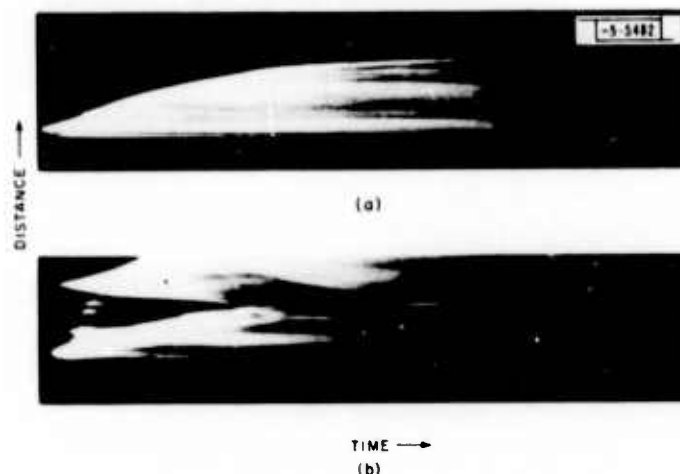


Fig. 1-10. Streak photographs of (a) plasma front generated by pulse 1, and (b) plasma front generated by pulse 2.

of the plasma-front motion for the first and second pulses are shown. The plasma-front motion away from the target for the first pulse is well behaved while for the second pulse several near simultaneous breakdowns are observed away from the target surface. The experiments reported here were done with no crossflow of air over the target. If the measurements were repeated with crossflow, the delay time required for "recovery" should be determined by the time it takes to clear the focal volume,

$$\tau_d \approx \frac{D}{v} \quad (1-21)$$

where D is the focal spot diameter and v is the crossflow velocity.

J. E. Lowder
L. C. Pettingill

2. Laser-Generated Electron Distribution in Front of Target

In the preceding Optics Research Report² the environment in front of a laser-irradiated target was characterized using visible interferometry and 10.6- μm crossbeam absorption. At the time of publication few interferograms had been reduced via Abelian inversion to 2-dimensional maps of optical refractivity, $(n - 1)/(n_0 - 1)$. In this section we have selected those data in which

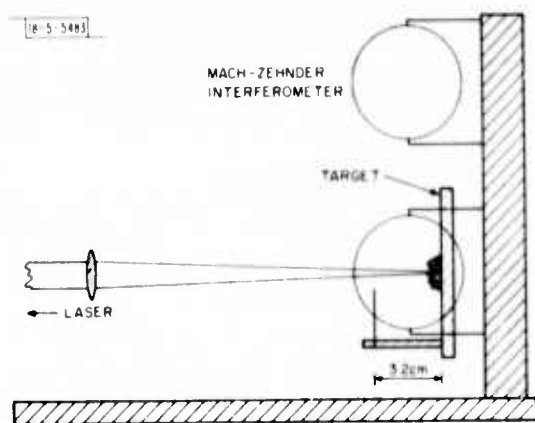


Fig. I-11. Geometry of laser target irradiation and interferometer observation.

the incident flux levels were 1 to 3×10^6 W/cm² or in the region where efficient thermal coupling has been reported on metallic targets.⁵ Interferograms typical of this regime (Figs. I-37(a) and (c) in Optics Research Report 1973-2) manifest spherical symmetry for $2 < t < \sim 90$ μ sec. Plots of the optical refractivity $(n - 1)/(n_0 - 1)$ as a function of Z , the distance normal to the target, characterize the entire hemispherical distribution. By combining data from instantaneous 2-dimensional interferograms and time-resolved streak interferograms the temporal evolution and decay of the surface plasma has been characterized.

The observation and irradiation geometry is illustrated in Fig. I-11. Three-mm-thick 2×2 -cm aluminum targets (uncleaned shop grade 2024) were used for all experiments. A typical laser pulse containing ~ 5 J in 40 to 50 μ sec is illustrated in Fig. I-32(b) in Optics Research Report 1973-2. The focal spot had a smooth profile with half-power diameter of 3.8 mm (0.11 cm²).

Figure I-12 is a plot of $(n - 1)/(n_0 - 1)$ as a function of Z for an average incident flux of 1.2×10^6 W/cm² at 5, 10, 15, 25, and 35 μ sec from the beginning of irradiation. Plasma formation occurred in < 1 μ sec during the initial gain spike. This instantaneous flux during the spike is 2 to 2.5 times the average during most of the pulse. The regions of negative refractivity, assumed to be purely electronic, are indicative of electron densities of $n_e \sim 2$ to 4×10^{18} cm⁻³ in a 3-mm sphere at 5 μ sec; at 25 and 35 μ sec, $n_e \sim 5 \times 10^{17}$ cm⁻³ and the radius of the electron-rich region has decreased from ~ 8 mm to ~ 5 mm at the longer observation time. In this irradiance regime the pressure wave generated at the target is a weak, nearly sonic ($< \text{Mach } 2$) disturbance.

After the laser irradiation has been terminated, the electron sphere decays slowly leaving in front of the target a hot low-density air and target vapor sphere with ~ 5 mm radius for this experimental geometry. These conditions are illustrated in Fig. I-13 for observation times 8, 22, and 45 μ sec after a 45- μ sec irradiation at $\sim 10^6$ W/cm².

The complexity of the physical processes taking place at the target makes analytic comparisons with theory difficult. Stamm and Nielson have constructed a computer program to consider a one-dimensional model of the laser target interaction in the thermal coupling regime (10^6 to 10^7 W/cm²) (Ref. 6). For an incident flux of 10^6 W/cm² they predict an electron density of $\sim 10^{18}$ cm⁻³ extending ~ 7 mm from the target surface at 12 μ sec. This prediction is bracketed by the data for 10 and 15 μ sec in Fig. I-12.

The data presented above illustrate a tenuous relatively thin electron-rich region near the surface of an aluminum target irradiated at 10^6 W/cm². The pressure disturbance is relatively

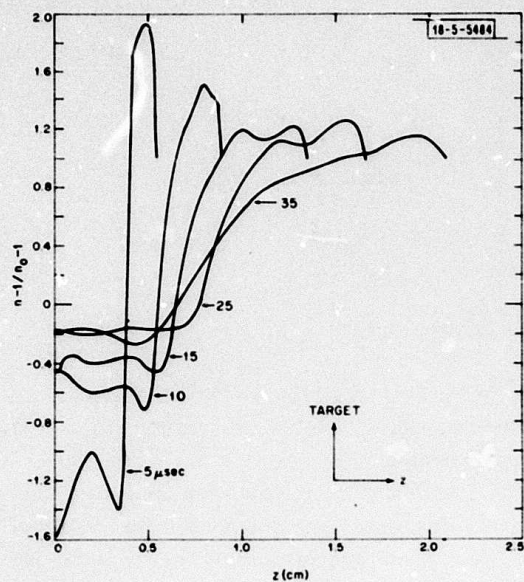
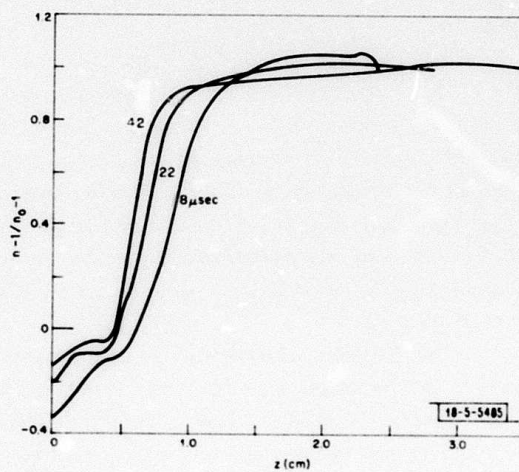


Fig. I-12. Plot of $(n - 1/n_0 - 1)$ as a function of perpendicular distance from an aluminum target for observation times of 5, 10, 15, 25, and 35 μ sec after beginning of laser pulse.

Fig. I-13. Plot of $(n - 1/n_0 - 1)$ as a function of perpendicular distance from an aluminum target for observation times of 8, 22, and 42 μ sec after the termination of irradiation.



weak ($< \text{Mach } 2$). It has been suggested that the presence of this electron-rich region explains some observation of enhanced thermal coupling in the $1 \text{ to } 5 \times 10^6 \text{ W/cm}^2$ irradiance regime.

R. W. O'Neil H. Kleiman
D. Mooney L. Pettingill

3. Fast Thermocoupling of Targets

An experimental program has been initiated to measure the heating of metallic surfaces due to irradiation with $10.6\text{-}\mu\text{m}$ laser radiation in both the presence and absence of plasma formation at the target surface. A copper target has been fabricated in which four fast-response ($\sim 10 \mu\text{sec}$) thin-film thermocouples were installed so that the surface temperature response of the target could be measured.

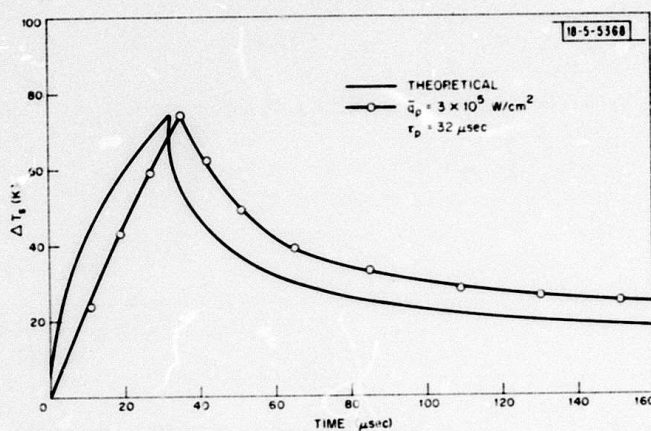


Fig. 1-14. Surface temperature history of 1/2-inch-thick copper target irradiated with a $10.6\text{-}\mu\text{m}$ laser pulse.

Some preliminary measurements of the surface temperature response in the absence of plasma formation have been made. The copper target was irradiated with a constant power density of $3 \times 10^5 \text{ W/cm}^2$ for $32 \mu\text{sec}$. The measured surface temperature response is shown in Fig. 1-14. The solid line is the theoretical surface temperature response when the surface absorptivity was chosen so that the peak temperature was the same for the theory and experiment. The surface absorptivity was approximately equal to 0.1 for this case.

Work is in progress on a computer program which will compute the actual surface heating rate from the measured surface temperature response and will be reported in the future.

J. E. Lowder
D. L. Mooney

C. DEVICES

1. H_2 -HF Laser

a. Introduction

The objective of this project is to obtain a long-pulse ($1 \text{ to } 5 \mu\text{sec}$) HF laser with 1 to 10 joules of output energy. An additional requirement is that the laser be sufficiently rugged and safe that it can be conveniently used for propagation or surface experiments.

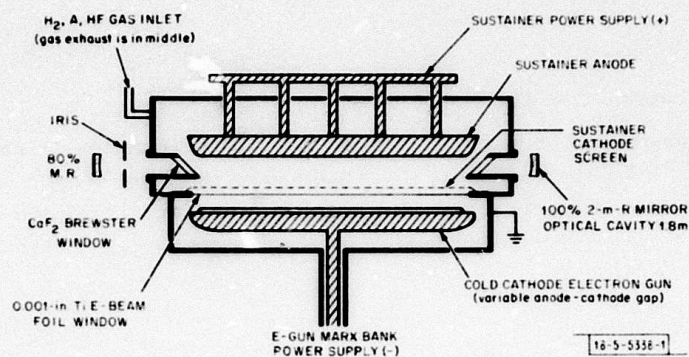


Fig. I-15. Schematic of experimental apparatus for H_2 -HF laser.

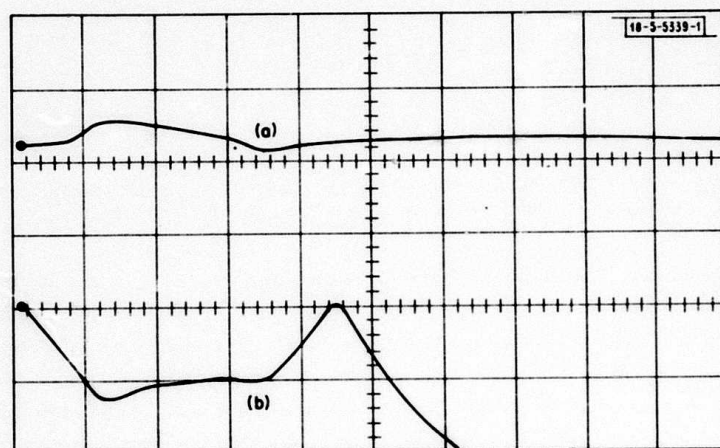


Fig. I-16. Photograph of temporal evolution of laser (a) and sustainer current (b). Pulse time scale is in $1 \mu\text{sec}/\text{div.}$

In this report, we describe the experimental work towards developing such a laser. The theoretical rationale behind our approach has been discussed in detail in the two previous Optics Research Reports.

We wish to emphasize that our approach, e.g., use of a cold-cathode-electron beam-stabilized discharge to pump an H_2 -HF mixture, is very much in the experimental-early development stage. With one recent exception,⁷ no other laboratories have reported laser oscillation in such a system. No previous reports of laser action at the high pressures and at the electric field to particle densities (E/N) ratios, which we have worked with here, have been made.

b. Experimental Apparatus

The electron beam system for this laser arrived from the vendor in late April several months behind schedule. Within three weeks after arrival the experimental apparatus shown in Fig. 1-15 was constructed. Of particular importance in this apparatus are the following: (1) the vacuum chamber and the gas flowing system were fabricated entirely of materials resistant to attack by HF, (2) the ultimate vacuum in this system was 40 microns with a leak (outgassing) rate of about 200 microns/half hour, (3) the system has gas supplies suitable for non-flowing static-fill gas mixture, (4) a capacitance monometer, having a dynamic range of 10^4 was used to monitor the pressures of the HF, H_2 , and A, and (5) both laser detectors were housed in a Faraday cage to eliminate stray noise arising from the electron beam gun.

Performance from the electron beam-sustainer discharge system was good. We were able to obtain reliable 3- μsec pulses of electrons with current densities of $\sim 1 \text{ A/cm}^2$ and energies of 200 keV. Within certain limitations, we were able to vary the beam pulse width from 0.5 to 5 μsec . Higher electron energies and currents could be obtained; however, in view of the tight schedule little effort was made to "push" the device to its maximum stated limits.

c. Experimental Results

The first experimental result was that the laser oscillates. Its output wavelengths are the HF 3- μm vibrational-rotational bands of interest to this program. This fact was confirmed by inserting an array of high- and low-pass optical filters in front of the detectors. In this manner the laser wavelength was bracketed to be between 2 and 3 μm . In addition, no laser oscillation was observed with HF absent from the gas mixture.

In another experiment, we confirmed that the small-signal gain of the medium was not so high as to allow for strong stimulated emission to occur without the presence of mirrors ("super-radiance" or superfluorescence). The absence of such very high gains means that extraction of a high-quality optical beam from a well-designed optical cavity is possible. Good beam quality is an important step in obtaining a high-brightness laser source.

One portion of the objective of this program is to produce an HF laser with a long (1 to 5 μsec) pulse width. Measurement of the laser pulse length was made with a suitable filtered InSb detector. As illustrated in Fig. 1-16, our measurements determined that the HF pulse length followed the sustainer current pulse (after a delay of about 1 μsec). Thus, the maximum laser pulse in our case was about 4 μsec — the duration of the maximum length e-beam pulse used in our experiments.

As mentioned in the previous subsection, the laser was operated with a static fill of the appropriate gas mixture. Despite the fact that various components internal to the sustainer box were not designed for high-vacuum, ultraclean conditions, sealed-off laser lifetimes of about

20 shots were obtained. This performance appeared to exceed the lifetime as seen in CO_2 laser-type mixtures which were subjected to similar testing. Long sealed-off lifetime is a significant advantage in designing a practical high-power laser. The "reusable" nature of the laser medium in this case makes this form of HIF laser an attractive alternative to the usual chemical HIF lasers - which by their very nature demand reusable gas flows.

The final experimental results concern the laser's efficiency and output power or energy. Output energy was measured by using a calibrated barium titanate detector. From this measurement and that of the pulse width, the laser pulse power could be determined. During the course of the power measurements it was determined that the existing optical cavity allowed energy extraction from only 0.1 liter. Thus, the total extracted energy was 1/25 of the total available optical energy. The results of the energy power measurements are summarized in Table I.

TABLE I ENERGY POWER MEASUREMENTS	
Gas mixture	8 HF, 80 H_2 , 800 Ar
Pulse width	2.5 μsec
Pulse energy	50 mJ
Peak power	8 kW
Efficiency	0.6 percent
Note: A maximum of 80 mJ was measured in a longer length pulse.	

Note that all measurements represent orders-of-magnitude improvement over those reported in Ref. 7. The figure of 2.2 joules potentially extractable energy is within the range stated in the objective of this work. With an appropriately designed optical cavity at least this much energy could be extracted.* Unfortunately such a design procedure would require knowing the gain and saturation power of this laser. However, after consideration of the time constraints on this program, an alternate approach - that of building different forms of HIF lasers - was employed. This approach is described in a succeeding section.

d. Summary of H_2 -HIF Laser

We summarize the salient results of this program as follows:

- (1) An HIF laser which operated on the principle of direct electron pumping of the laser medium has been designed and given preliminary testing.
- (2) The laser gain is workably high - but not so high that the laser exhibits "super-radiant" output.

*Undoubtedly, the figure could be improved if gas mixture, mirror reflection, etc., were improved.

- (3) If the laser is sealed off, a given gas fill has been observed to exhibit laser action for 20 or more shots. Considering the vacuum properties of the system, this performance indicates long sealed-off lifetimes with the system are possible.
- (4) The unoptimized, extractable, optical energy from the laser medium is about 1.2 joules/liter. However, due to limitations imposed by the existing optical cavity, only a fraction of the available energy was extracted.

R. M. Osgood
D. Mooney
A. J. Morency

2. Long-Pulse HF Chemical Laser

An alternate and simple approach to obtaining a 1- to 5- μ sec 1- to 10-joule HF laser pulse is to use a long-pulse, cold-cathode e-beam to induce a chemical reaction in an SF_6 - H_2 gas mixture. The basic physics of such a laser are similar to those of a TEA or shortpulse e-beam-initiated SF_6 - H_2 hydrogen fluoride laser. The fluorine for the inverting process of $\text{H}_2 + \text{F} \rightarrow \text{HF}$ ($V = 3, 2, 1$) + H is created by disassociative attachment of the SF_6 by thermal electrons or by direct molecular fragmentation by high-energy electrons.

In this experiment, the cold-cathode electron gun from the Systems, Science, and Software laser system (described in the previous section) was used to provide the source of high-energy electrons. Earlier computer studies had shown that HF laser emission from such an irradiated mixture would exhibit the same approximate time behavior as the electron beam pulse. This point is illustrated in Fig. I-17 which shows the temporal evolution of the laser pulse during application of a triangular, 3- μ sec electron beam pulse. Note that, since the cold-cathode e-beam pulse width is variable from 1 to 5 μ sec, the laser pulse from such a device should also be variable in a similar matter.

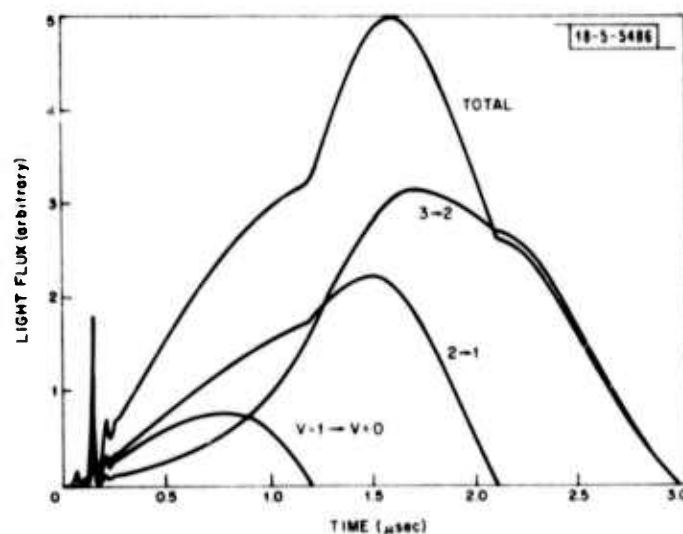


Fig. I-17. Computer plot of temporal evolution of laser pulse in a transverse e-beam-initiated HF chemical laser.

Because of the high gain in HF chemical lasers, beam quality from this laser will be somewhat degraded from that obtainable in the H_2 -HF laser. However, because of the high gain, laser energy can be extracted from the entire excitation volume with existing optical components. Further, since the irradiating beam is transverse to the optical axis, it is a simple matter to use an optical cavity to insure reasonable beam quality. Employment of an optical cavity is not such a simple matter in SF_6 - H_2 lasers with e-beam excitation along the optical axis.

At the writing of this report we have obtained the following results:

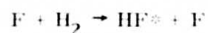
- (a) With a static fill the repetition rate is about one shot per four minutes. With a flowing system one shot per minute is possible.
- (b) Pulse length variable from 1 to 3 μsec . No testing at longer duration e-beam pulses has been attempted.
- (c) Laser energies of one joule were obtained. It appears a straightforward matter to increase these energies to 4 to 5 joules. This can be done by working at higher e-beam currents, and optimizing the gas mixture.

R. Osgood
D. Mooney
S. Marcus

3. Electron-Beam-Initiated HF Laser

In April of this reporting period, the electron beam accelerator (Pocobeam), used to initiate our chemical HF laser, was delivered by Maxwell Laboratories. In addition, fabrication of the laser tube and associated parts was completed, and the laser is presently in operation.

In the laser, shown in Fig.1-18, the 500-keV electron beam is injected longitudinally down the optical axis initiating the reaction



which produces an intense superradiant infrared pulse. Cavity mirrors are not required for this device.

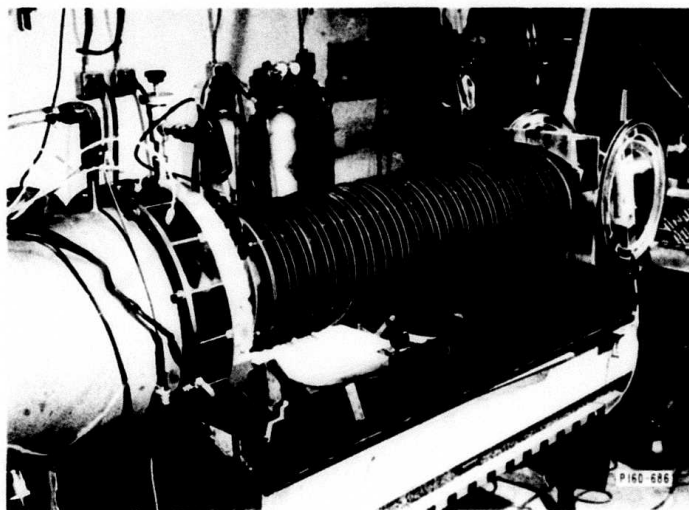
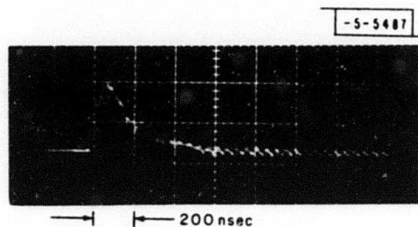


Fig.1-18. Electron-beam-initiated HF chemical laser.

Fig. I-19. Laser pulse shape as recorded with InAs detector; time scale 20 nsec/div.



With a gas mixture of 70 torr SF_6 and 10 torr C_2H_6 , the laser output has been measured at 20 joules. The pulse width, as measured by a room-temperature InAs detector, is 200 nsec. A typical pulse is shown in Fig. I-19. The pulse width can be varied somewhat by changing the reactant pressures. The observed pulse shapes agree with those predicted by our HF kinetics code. Currently, the laser is being used to perform surface effects experiments.

S. Marcus D. L. Mooney
R. C. Archibald J. F. Bushee

4. HF Electric Discharge Laser

During this period, efforts were continued to measure the energy output of our HF electric discharge laser. To accomplish this, the device was scaled up in both size and energy input. A 750-joule Marx bank was obtained commercially, and a laser chamber with an active volume of $7 \times 7 \times 125$ cm was constructed. As a result, the energy output was increased from 2.25 to 6.0 joules. Further increases in energy output can be expected by minimizing the Marx bank inductance.

S. Marcus

5. Progress in CO_2 Isotope Lasers

We have obtained a very large number of lasing transitions in $^{16}\text{O}^{12}\text{C}^{18}\text{O}$ and in $^{16}\text{O}^{13}\text{C}^{18}\text{O}$ lasing mixtures. Both even and odd rotational levels have been observed, as expected for a linear molecule in which one atom is replaced by an isotopic atom.

Optical and microwave heterodyne techniques were used to generate and measure difference frequencies between a stabilized isotope and a stabilized $^{12}\text{C}^{16}\text{O}_2$ reference laser. As an example, Fig. I-20 shows the 24,410.301-MHz beat frequency of the $^{16}\text{O}^{12}\text{C}^{18}\text{O}$ 001-I P(12) and the $^{12}\text{C}^{16}\text{O}_2$ 001-I P(6) transitions. The 52-dB signal-to-noise ratio indicated for the 24.4-GHz beat note shown in Fig. I-20 is a typical value that can be obtained by using varactor-photodiode detection techniques⁸ with the high-speed, high quantum efficiency HgCdTe photodiodes developed by D. L. Spears.⁹

The measured difference frequencies were fitted in a least-squares sense to the expansion of the line frequencies

$$\begin{aligned} f = f_0 + B_u [J'(J' - 1) - J(J + 1)] - (B_l - B_u) J(J + 1) \\ - D_u [J'^2(J' + 1)^2 - J^2(J + 1)^2] + (D_l - D_u) J^2(J + 1)^2 \\ + H_u [J'^3(J' + 1)^3 - J^3(J + 1)^3] - (H_l - H_u) J^3(J + 1)^3 \end{aligned}$$

where $J' = J - 1$ for a P(J) line and $J' = J + 1$ for a R(J) line. The $^{12}\text{C}^{16}\text{O}_2$ reference frequencies were computed from the published constants.^{10,11}

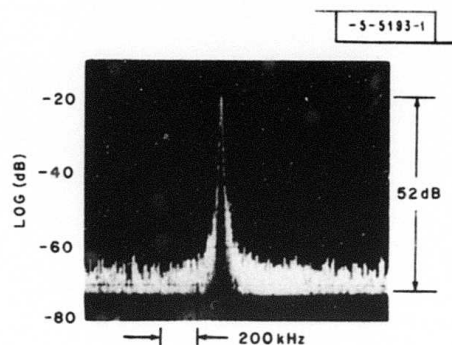


Fig. I-20. 24,410.301-MHz beat of $^{16}\text{O}^{12}\text{C}^{18}\text{O}$ laser 001-I P(12) and $^{12}\text{C}^{16}\text{O}_2$ laser 001-I P(6) transitions. Power levels into photodiode: $^{12}\text{C}^{16}\text{O}_2$ laser: 0.42 mW, $^{16}\text{O}^{12}\text{C}^{18}\text{O}$ laser: 0.48 mW. Second harmonic of microwave LO, 10-kHz noise bandwidth.

The band centers and rotational constants of $^{16}\text{C}^{12}\text{C}^{18}\text{O}$ which we determined represent a 10^5 -fold improvement over the data previously published for this isotope.

Improvements in our grating-controlled laser design and active stabilization to external, low-pressure room-temperature CO_2 reference cells enabled us to obtain many more lasing transitions and 10^3 times better frequency accuracy when compared to the results we recently published¹² on $^{12}\text{C}^{18}\text{O}_2$, $^{13}\text{C}^{16}\text{O}_2$, and $^{13}\text{C}^{18}\text{O}_2$ isotope lasers.

In the present experiments we are using statistical equilibrium mixtures of $^{12}\text{C}^{16}\text{O}_2$, $^{16}\text{O}^{12}\text{C}^{18}\text{O}$, $^{12}\text{C}^{18}\text{O}_2$, and $^{13}\text{C}^{16}\text{O}_2$, $^{16}\text{O}^{13}\text{C}^{18}\text{O}$, $^{13}\text{C}^{18}\text{O}_2$ molecules. As a consequence, several hundred lasing transitions were obtained from a single CO_2 laser. Insofar as sealed-off operation is concerned, the experience we have so far accumulated indicates that the pure isotopes and the statistical equilibrium mixtures are quite comparable to standard CO_2 lasers.

In conclusion, the development and calibration of stabilized CO_2 isotope lasers will provide hundreds of precisely known, easily resettable frequency reference comb lines over the entire 8- to 12- μm spectrum.

It is also noteworthy that many of the $^{16}\text{O}^{12}\text{C}^{18}\text{O}$ lasing transitions occur almost precisely half way between the most dominant $^{12}\text{C}^{16}\text{O}_2$ lines. This is an important consideration both in high-pressure continuously tunable CO_2 lasers and also in the design of multiline, short-pulse, high-energy systems to be used in fusion experiment.

C. Freed
A. H. M. Ross
R. G. O'Donnell

REFERENCES

1. D. E. Lencioni and H. Kleiman, "Effects of Aerosol Particle Heating on Laser Beam Propagation," Project Report LTP-27, Lincoln Laboratory, M.I.T. (22 July 1974).
2. Optics Research Report, Lincoln Laboratory, M.I.T. (1973-2), DDC AD-779917.
3. R. W. O'Neil, H. Kleiman, L. C. Marquet, C. W. Kilcline, D. Northram, *Appl. Opt.* 13, 314 (1974).
4. J. E. Lowder, D. E. Lencioni, T. W. Hilton, R. J. Hull, *J. Appl. Phys.* 44, 2759 (1973).
5. R. R. Rudder and R. L. Carlson, "Material Response to Repetitively Pulsed 10.6 Micron Laser Radiation," AFWL-TR-74-100, Air Force Weapons Laboratory (May 1974).
6. M. R. Stamm and P. E. Nielson, "Thermal Coupling in Multiply Pulsed Laser Target Interactions," AFWL-TR-74-100, Air Force Weapons Laboratory (May 1974).
7. S. Byron, L. Nelson, G. Mullaney, *Appl. Phys. Lett.* 23, 565 (1973).
8. D. L. Spears and C. Freed, *Appl. Phys. Lett.* 23, 445 (1973).
9. D. L. Spears, T. C. Harman and I. Melngailis, Proceedings of the IRIS Detector Specialty Group, Washington, D. C. (13-15 March 1973).
10. K. M. Evenson, J. S. Wells, F. R. Petersen, B. L. Danielson and G. W. Day, *Appl. Phys. Lett.* 22, 192 (1973).
11. F. R. Petersen, D. G. McDonald, F. D. Cupp and B. L. Danielson, *Phys. Rev. Lett.* 31, 573 (1973).
12. C. Freed, A. H. M. Ross and R. G. O'Donnell, *J. Mol. Spectry.* 49, 439 (1974).

II. OPTICAL MEASUREMENTS AND INSTRUMENTATION

A. INTERFEROMETRIC IMAGE EVALUATION

1. 10.6- μm MTF Measurement

In order to test the operation of an infrared triangular scanning interferometer,¹ the beam splitter and the shear plate in the laboratory system were exchanged for barium fluoride (beam-splitter) and germanium (shear-plate) components, coated for 10.6- μm infrared operation. A pyroelectric detector replaced the photomultiplier. A GTE Sylvania 941S CO_2 laser beam at 10 μm was expanded to a 50-mm-diameter beam, and this was then stopped down to a 10-mm diameter before entering the interferometer. A helium neon laser beam was used for preliminary alignment. The slow-speed scanning motor drive was used. The resultant MTF curves, examined on an oscilloscope display, are shown in Fig. II-1. The top display was traced at a speed of 1.0 sec per division, the lower curves expanded to 0.2 sec per division. The MTF curves are essentially the diffraction-limited curve for a clear circular aperture. Good clean signals were obtained (no noise), but a small ghost signal is present outside the main MTF curve, presumably due to the ghost reflections from the optics caused by optical coating limitations. This can be improved, but the test demonstrated the feasibility of the infrared system, and an engineered unit is being built.

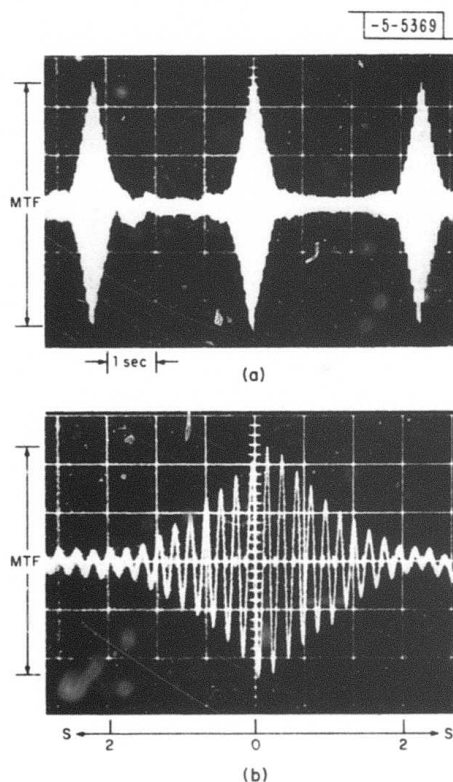


Fig. II-1. Laboratory interferometer MTF output at 10.6 μm . (10-mm beam with Ge shear plate and BaF_2 beam splitter). (a) MTF output, (b) expanded shear scale.

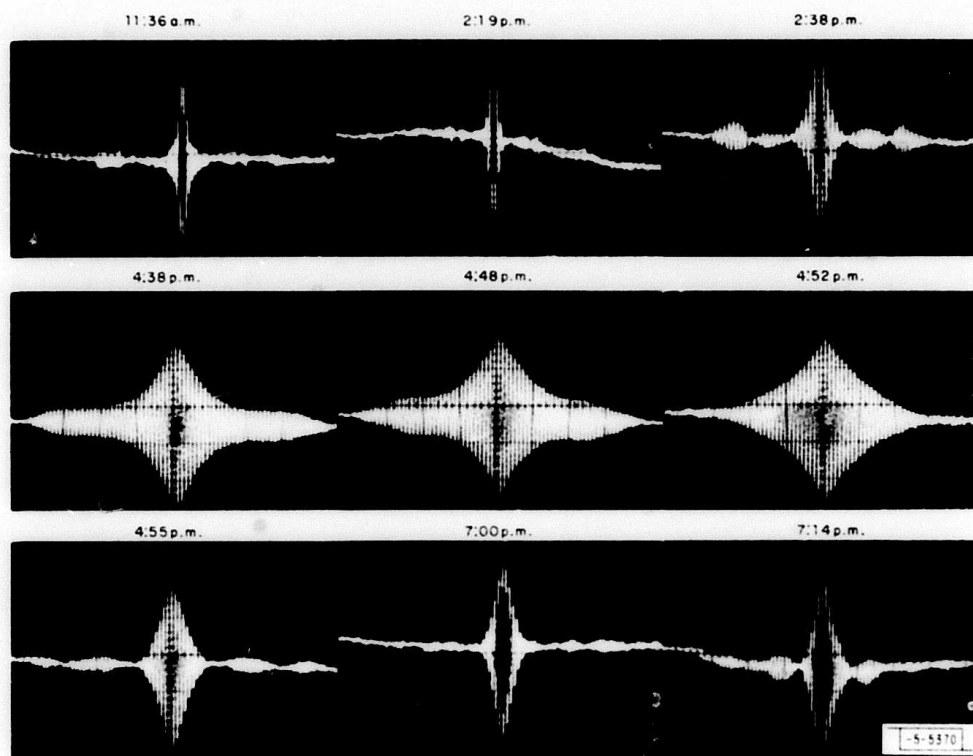


Fig. II-2. 178-mm Questar MTF measurements over 600-m ground range (HeNe laser) selected at various times during the day (each pair of curves taken in 2 msec).

2. Visible Region, 600-Meter-Range MTF Measurements

The visible FSI was tested over a horizontal path of 600 meters at the ATR (Antenna Test Range), and MTF data recorded during a typical day on an FM magnetic tape recorder. Figure 11-2 shows a selection of pairs of MTF data selected at both high- and low-turbulence times during the day. The shape of the curve represents the turbulence or seeing conditions, and each pair of MTF curves is completely scanned in 2.5 msec. The curves shown are "typical" at the time indicated. Thus, the best seeing (highest MTF) is around 4:38 and 4:48 p.m. on this particular day, 6 March 1974, and at this time, is virtually diffraction limited. By 4:55 p.m. it has started to deteriorate. By 7:00 p.m. it is much poorer, but not as poor as late morning or around noon-time. If at one particular time (say, around 7:20 p.m.) the MTF curves are examined as shown in Fig. 11-3, it is seen that the shape, while fairly constant over a 2.5-msec time interval (each MTF curve is fairly symmetrical), changes quite drastically over 8 msec. From one minute to the next, dramatic changes are evident. Clearly, individual curves at one instant of time are only an approximate guide to the imaging properties of the propagation path. This type of data can only be evaluated in a statistical sense. Attention must be given to different integration times. Over other propagation paths or conditions, the rapidity of changes in the seeing may be slower or faster. An understanding of these changes is essential if imaging of an object or the propagation of a laser beam is to be carried out with the best results. In some cases, a "seeing monitor" (e.g., a continuously operating interferometer) will be essential; in other cases, a statistical description of the propagation conditions will be necessary to properly determine the imaging characteristics for given time intervals of a particular atmospheric path. Nearly one million MTF curves can be measured in an hour. Statistical analysis of the data, in which mean MTF, variances, and other properties of the data can be evaluated for different integration intervals, is therefore being investigated. The data shown in Figs. 11-2 and -3, taken with a 178-mm-diameter Questar receiving telescope, are typical samples selected (almost randomly) from a large amount of recorded data to illustrate the nature of the MTF results obtained on imaging through the atmosphere.

3. Long-Path (Star-Source) Atmospheric MTF Measurements

The FSI has been used to obtain MTF measurements through the atmosphere from the ground (with the 178-mm Questar telescope), pointing at a star source (Sirius). These data have not yet been examined in any detail. In addition, the interferometer was mounted at the focal plane of the 91.5-cm Cassegrainian telescope aboard the NASA Ames C-141 airborne observatory, and MTF data taken both on the ground and cruising at normal altitude and speed, tracking both Arcturus and Vega at different times during the night. Visual examination of the sheared interferogram was possible without any filters (i.e., "white-light" fringes). For this visual check, the telescope was defocused, and only at very small shear values (s below 0.1) could fringes be seen (and were photographed). After carefully focusing the telescope, MTF data were recorded on magnetic tape. One sample of the preliminary flight data is reproduced in Fig. 11-4(a). For comparison, a laboratory-produced white-light source (tungsten lamp) MTF is reproduced in Fig. 11-4(b). No spectral filters were used here. The photomultiplier had an S-4 cathode, the tungsten source was operated at a color temperature of about 2850 K. Clearly, the spectral bandwidth is so wide that the MTF in Fig. 11-4(b) falls off (limit below $s = 1.6$) significantly because of the spectral coherence loss. However, in Fig. 11-4(a) (Vega has a color temperature

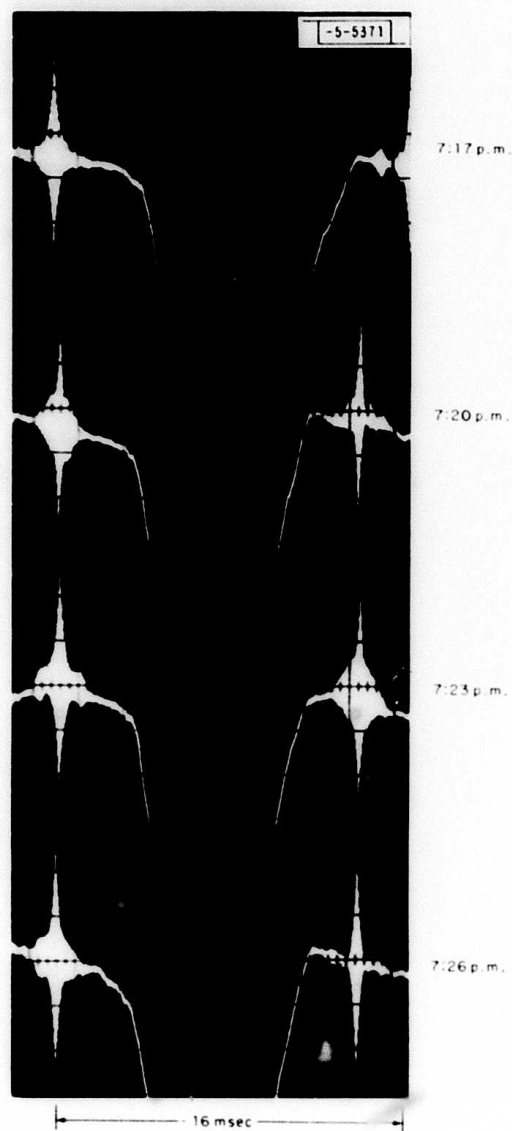
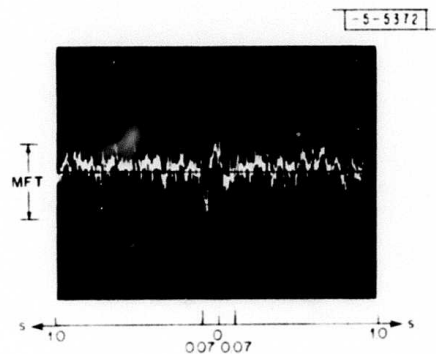
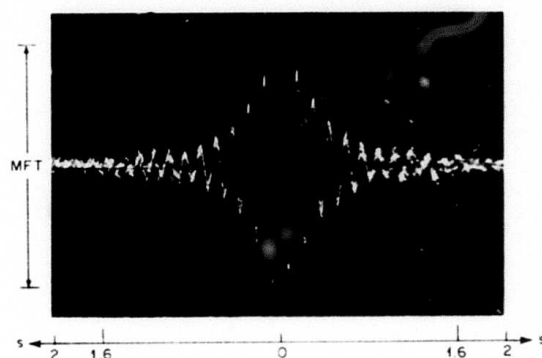


Fig. II-3. 178-mm Questar MTF measurements over 600-m ground range (HeNe laser) at about 7:15 p.m. showing rapid change over 16-msec time interval.



(a)



(b)

Fig. 11-4. Measured MTF from C-141 airplane in flight and ground calibration MTF in laboratory with white light. (a) Star (Vega) source; C-141 flight, 41,000 ft altitude, speed $M = 0.75$, 91.5-cm-diam. telescope, elevation $53^\circ 54'$. (b) White-light (tungsten source), 8.9-cm-diam. telescope, 14-m path.

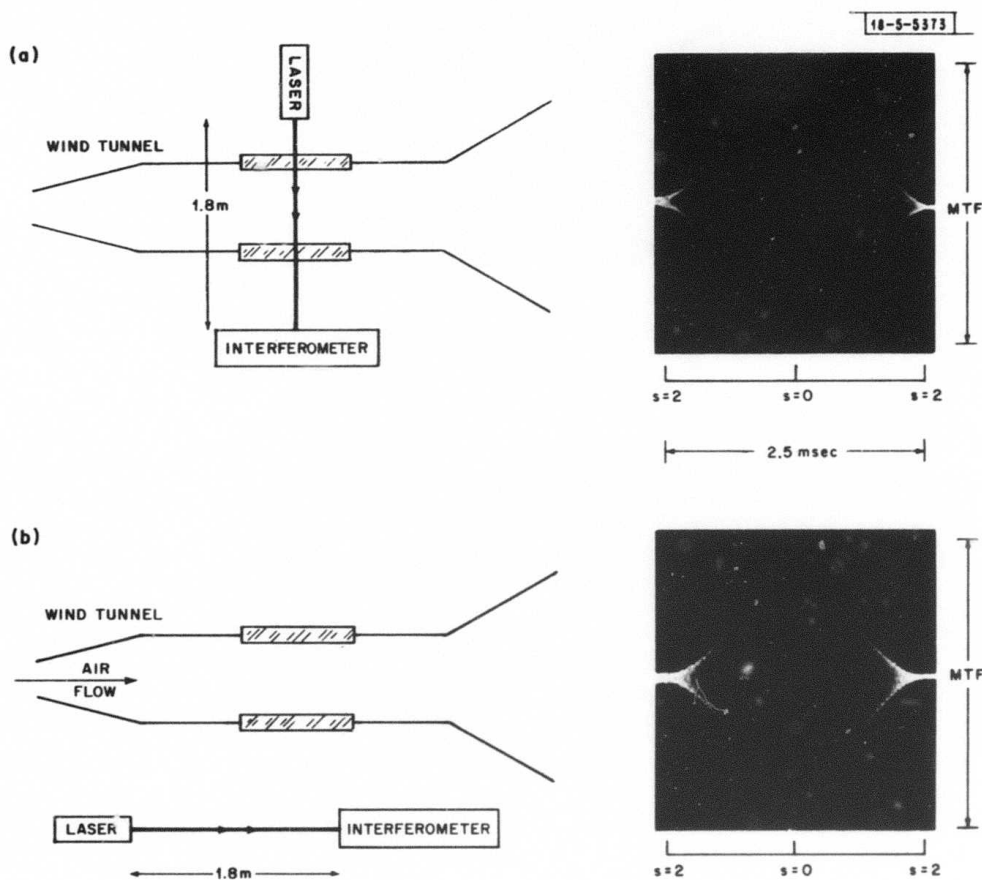


Fig. II-5. Calibration MTF measurements with 25-mm-diam. laser beam in the USAFA trisonic wind tunnel; (a) Tunnel off, pumps off, laser beam through tunnel. (b) Tunnel on ($M = 0.86$), pumps on, laser beam outside tunnel.

about 11,000°K), the carrier frequency signal was fairly small (only 1 cycle) and the MTF extent is about $s = 0.07$, so that over this small data region there has been little loss of signal due to coherence limitations. For better seeing conditions, narrowband filters must and have been used in other experiments. This comparison serves simply to confirm that in the star measurement, the MTF is not being degraded by the spectral coherence limitations over the range of MTF modulations recorded here. (This point, while demanding more clarification, will be analyzed more completely at a later date.) The data on tape have not yet been analyzed. A limited number of photographs were taken of the sheared interferogram and of the star images, and only some very rough conclusions, tentative at this time, can be reported after a "quick look" at some of the data.

The FSI interferometer was easily operated in flight conditions, and both a stable interferogram and a characteristic MTF (which varied with time) were observed and recorded. The data indicate that a boundary-layer degradation is present, whose magnitude is apparently of the same order as was observed earlier on the KC-135 flight measurements previously reported.² This conclusion is, of course, tentative until the data have been more carefully analyzed, and will be reported at a later date.

4. Wind-Tunnel MTF Measurements

Some preliminary MTF measurements propagating a 25-mm-diameter laser beam through the test section of four different wind tunnels have been carried out using the FSI. These experiments were performed to assess the optical characteristics of several tunnels under normal operating conditions. The laser beam was directed through the respective Schlieren windows through the tunnel test section, and the emergent beam was received by the interferometer. A Spectra Physics 50-mm-diameter beam expander fitted to a HeNe laser produced the 50-mm-diameter test beam. This overfilled the 25-mm Spectra Physics collimator, which was fitted to the front of the interferometer. The received beam was thus limited to 25-mm diameter, being then reduced by this second collimator to about 8-mm diameter before entering the interferometer. All final focusing was done electro-optically by maximizing the overall MTF curve. The data for a number of different operating conditions (e.g., Mach number) were recorded on tape.

Samples of some of the data are reproduced here from four different wind tunnels, shown in Figs. 11-5 to -9. In all cases, a calibration run was made with the tunnels off to check that diffraction-limited performance was obtained, Fig. 11-5(a), thereby checking the wind-tunnel windows, the optics, and the alignment. In addition, several runs were made, not through the wind-tunnel test section but alongside the tunnel, with the tunnel and pumps or other machinery running at normal speed, to check that vibration or acoustical noise did not upset the MTF measurements, Fig. 11-5(b). In all cases, diffraction-limited performance was obtained (the propagation path being outside the wind tunnel), confirming that the noisy environment did not disturb the measurement, as shown in Fig. 11-5.

The four wind tunnels (W.T.) for which data were obtained are:

- | | |
|--|---------------------|
| (a) the USAFA 1 × 1-foot trisonic W.T. (a blow-down tunnel), | |
| (b) the NASA Ames 6 × 6-foot supersonic W.T., | } (all closed-loop) |
| (c) the NASA Ames 11-foot transonic W.T., | |
| (d) the NASA Ames 14-foot transonic W.T. | |

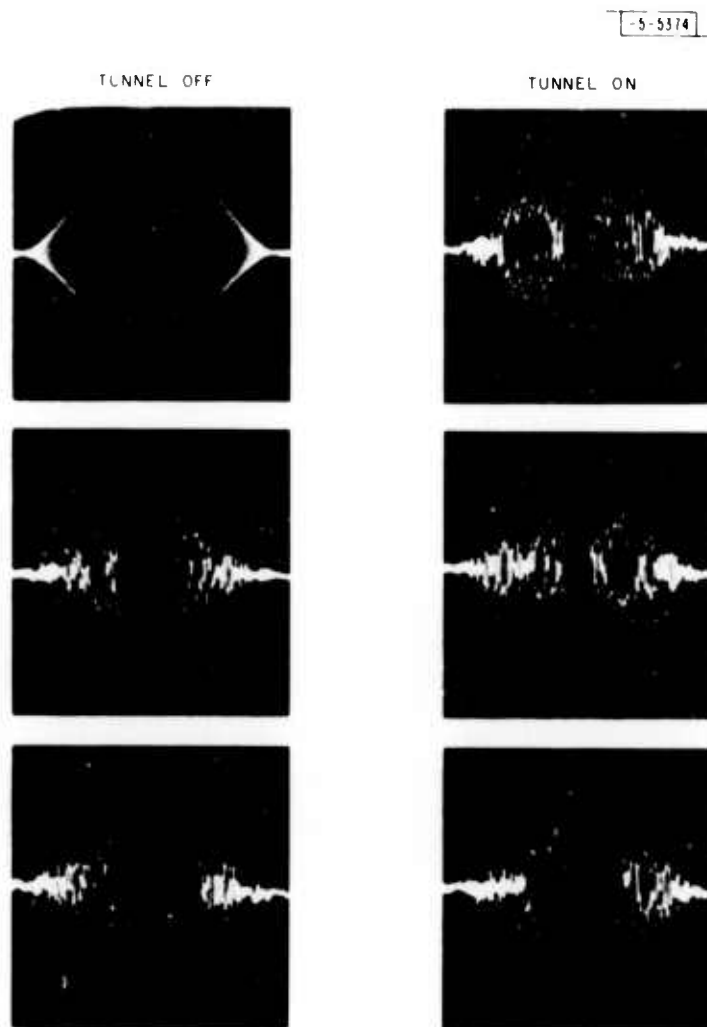


Fig. II-6. MTF measurements in USAFA trisonic wind tunnel at Mach 0.86 (25-mm HeNe beam).

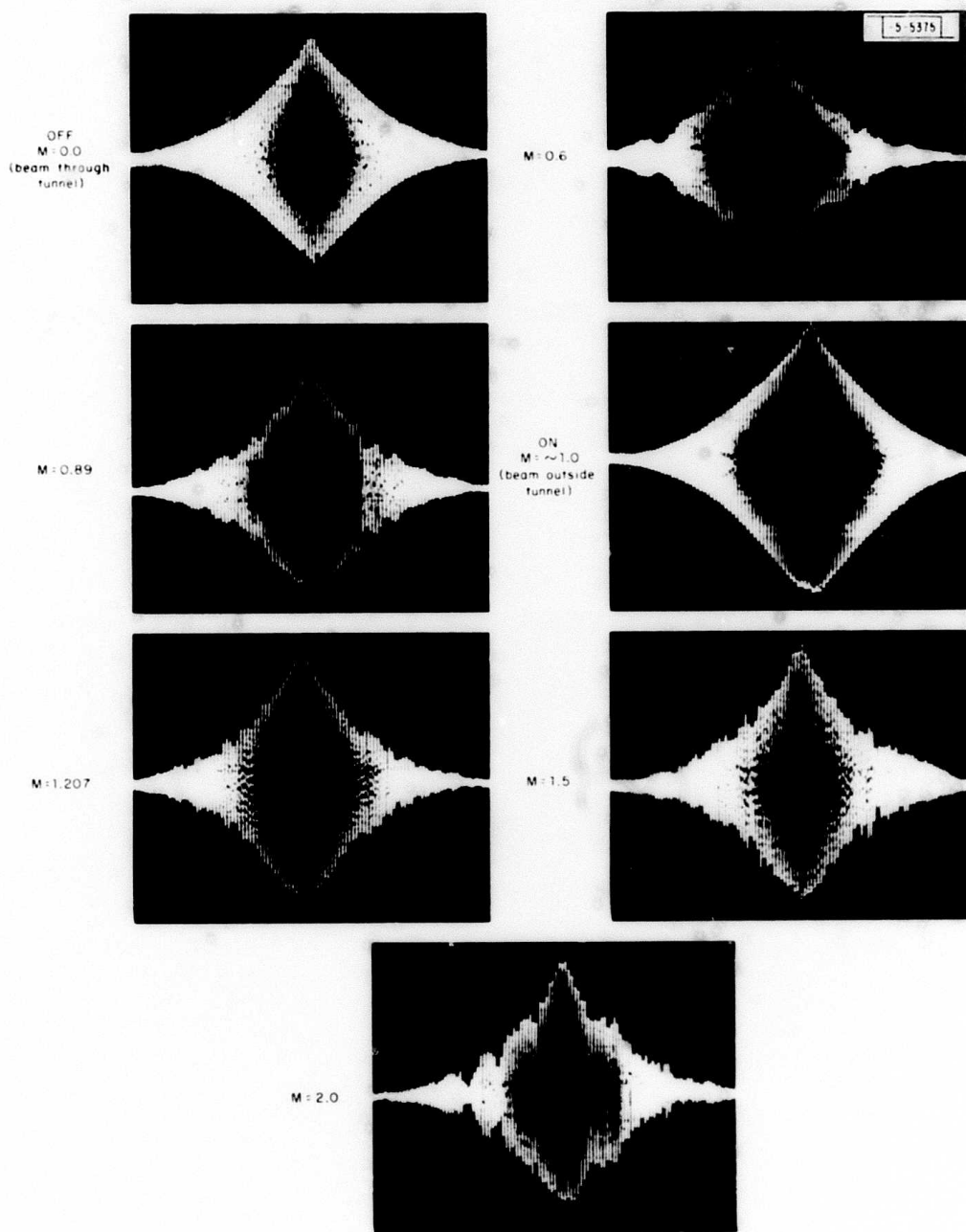


Fig. II-7. MTF measurements in NASA Ames 6-ft supersonic wind tunnel at various wind speeds (25-mm HeNe beam).

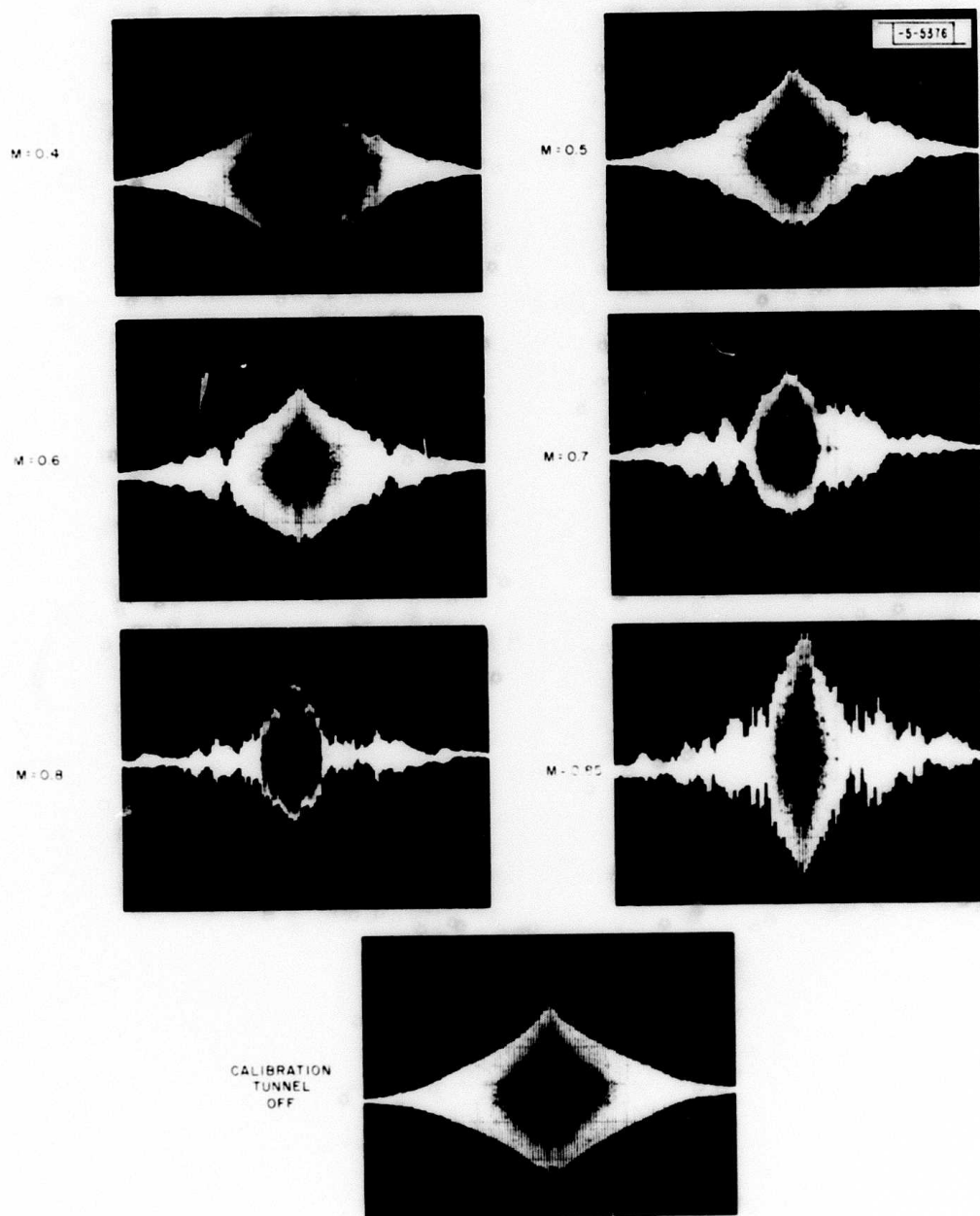


Fig. II-8(a). MTF measurements in NASA Ames 6-ft supersonic wind tunnel at various wind speeds (25-mm HeNe beam). (Note: ceiling and floor slots were taped up and $P_t = 30$ inches Hg.)

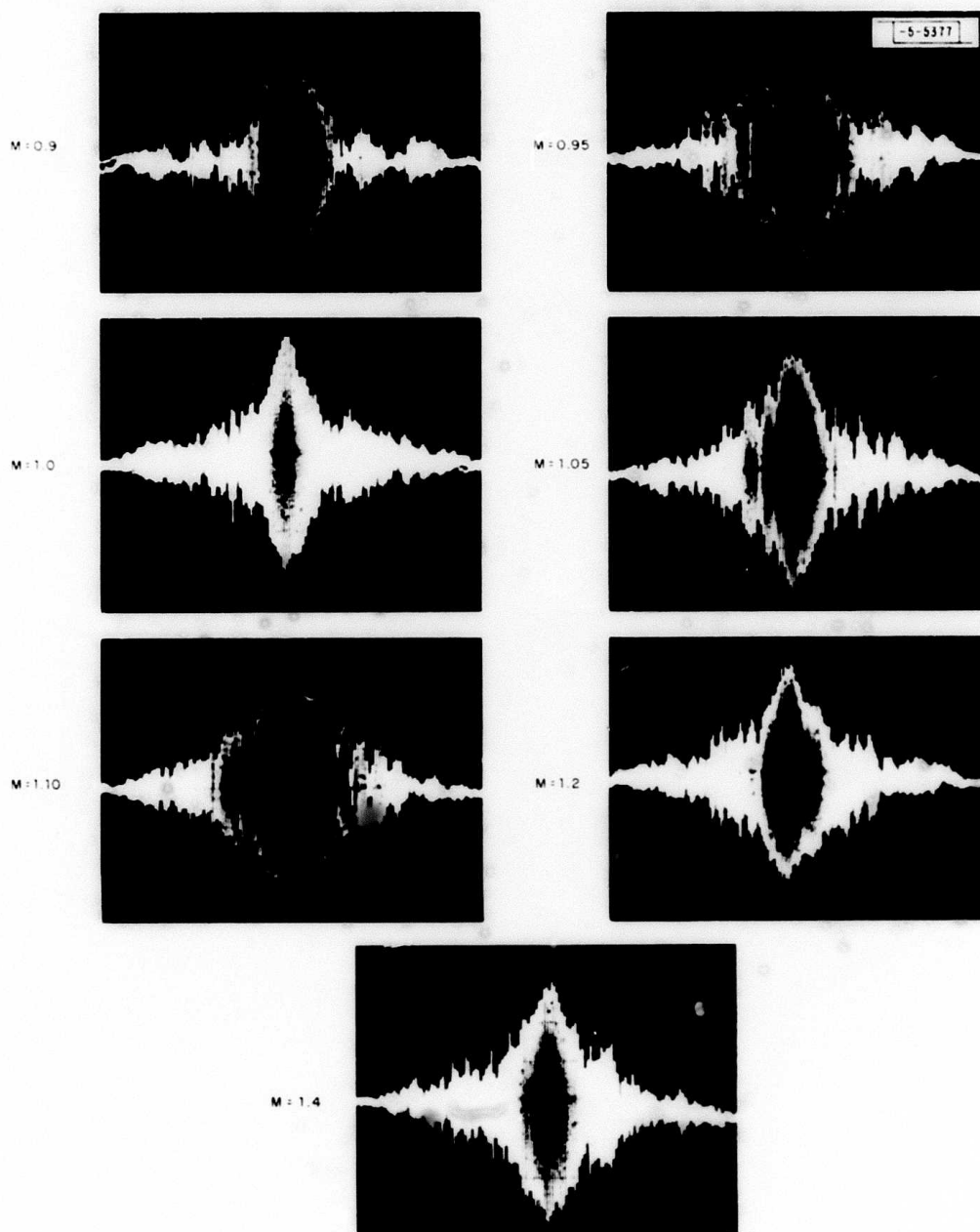


Fig. II-8(b). MTF measurements in NASA Ames 11-ft transonic wind tunnel at various wind speeds (25-mm HeNe beam). (Note: ceiling and floor slots were taped up and $P_t = 30$ inches Hg.)

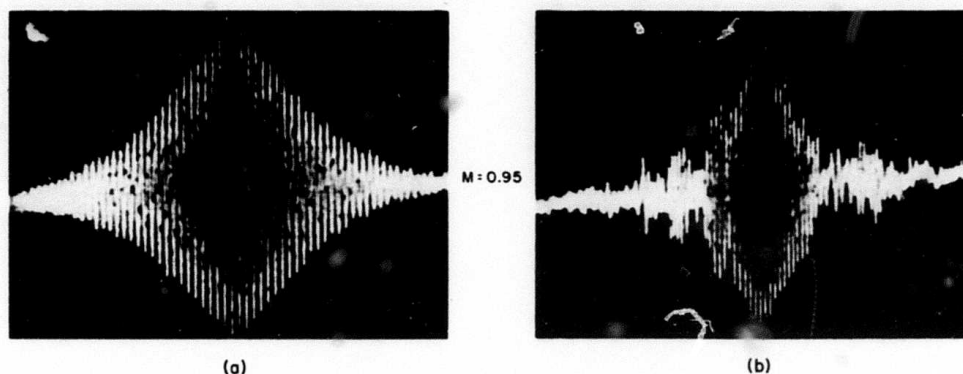


Fig. II-9. MTF measurements in NASA Ames 14-ft transonic wind tunnel at Mach 0.95: (a) Calibrate, beam outside tunnel; (b) beam through tunnel.

The first tunnel (Fig. II-6) showed fast and large fluctuations in the MTF, probably due to the temperature fluctuations induced in the air as it expanded from the pressure chamber. (This USAFA blow-down tunnel was open ended and quite different in operation from the three others tested.)

None of the NASA tunnels (all closed-loop) showed the same large variations as the USAFA blow-down tunnel. In fact, the 6×6 -foot tunnel was excellent and essentially diffraction-limited at all speeds to Mach 2.0, as indicated in Fig. II-7. However, the 11- and 14-foot tunnels both showed (Figs. II-8 and II-9) some significant MTF fluctuations, and more degradation was observed around Mach 0.85 in the case of the 11-foot tunnel than at either a higher or lower wind speed. These latter two tunnels both had a slotted test section with a large (about 3-foot) plenum cavity region on either side of the test section. The test beam had to traverse this plenum space on entering and leaving the test section. It is possible that the turbulent degradation may arise in this plenum space in the experiments done through both the 11- and 14-foot W.T. test sections. The 6×6 -foot W.T. had no such plenum cavity region. The position will need to be clarified by further tests.

Nonetheless, it is evident that optical properties of tunnels can be readily evaluated, and while a number of other tests have been done to date, the data have not yet been analyzed. However, simple, very useful evaluations are possible from a "quick look" at the data. One tunnel (the 6×6 -foot supersonic W.T.) has been found to be much cleaner than any other tunnel tested (and, in fact, essentially diffraction-limited for this size aperture, 25.0 mm in the visible region). The other tunnels each exhibited well-defined characteristic degradations, and these data are being analyzed.

5. Conclusion

A series of different measurements and applications using the FSI interferometer have been pursued, and a very large amount of data is being collected. Since data analytical techniques have not yet been properly developed, only a brief outline of the data collected to date has been reported here, together with some conclusions that must be regarded as tentative. Nevertheless, this very discursive and incomplete account of the measurements made with the interferometer

in the last few months demonstrates the ease with which data can be obtained. It is believed that "quick-look" examination of the real-time data provides a first good indication of the characteristics of the atmospheric imaging (or propagation) properties in question. However, a great deal of more detailed data analysis is required, from which a more rigorous set of conclusions can be expected.

D. Kelsall

B. LONG-PATH MONITORING OF ATMOSPHERIC CARBON MONOXIDE BY A TUNABLE DIODE LASER SYSTEM*

A tunable diode laser system has been developed to measure average ambient concentrations of carbon monoxide over an outdoor path of 610 meters. The preliminary system capability corresponded to a minimum detectable CO concentration of 5 parts per billion (ppb) with an integration time of one second.

The laser source of the monitoring system was one of the lead-salt diode laser types,^{3,4} which have been found to have inherent advantages, such as small size and ease in wavelength tunability, compared to other types of tunable lasers. In this system, a $\text{PbS}_{1-x}\text{Se}_x$ laser was chemically tailored ($x = 0.185$) to operate in the 2100-cm^{-1} frequency region ($4.7\text{-}\mu\text{m}$ wavelength range), in close coincidence with the fundamental vibrational band of CO centered at 2145 cm^{-1} (Refs. 5, 6). Exact frequency matching and tuning through the CO absorption lines were easily achieved by varying the injection current, which changes the junction temperature and thus the laser wavelength.

The detection technique used for measuring the CO concentration was that of resonance absorption.^{7,8,9} The laser was first tuned to an appropriate CO absorption line and derivative detection⁷ of this line was performed to measure the integrated CO concentration over the path.

The primary innovation in the present diode laser system was utilization of a commercially available, closed-cycle cryogenic cooler¹⁰ instead of the conventional liquid-helium dewar to provide the proper operating temperature ($\sim 15^\circ\text{K}$) for the diode lasers. Elimination of the liquid-helium requirement was a dominant factor in extending well-established, laboratory-based, diode laser spectroscopic methods into the practical field system reported here.

Carbon monoxide is an important pollutant in the ambient environment today, especially in metropolitan areas where the density of automobiles is high. (The CO content of automobile exhaust can be as high as 10 percent by volume.) In addition to their toxic effects, CO molecules play an integral part in the formation and conversion of other pollutants such as NO, O_3 and NO_2 (Ref. 11). Traditionally, the amount of CO in ambient air has been measured by point-sampling instrumentation based on conventional infrared techniques. However, the limitations of these point-sampling methods become obvious in cases where average pollution concentrations over a large area are desired. Thus, the long-path tunable laser system to be described here represents a development in the direction of a versatile, remote, and reliable air-monitoring system for that purpose.

Field measurements with our tunable laser system were performed in an old antenna range on the west side of Hanscom Field, Bedford, approximately 20 miles west of Boston and 2 miles northwest of Route 128. The site has small buildings, which contain the laser system and associated equipment, at each end, separated by 205 meters. The floors of these two buildings are made of concrete, providing some vibrational stability.

*This report describes the work performed at Lincoln Laboratory under the sponsorship of the National Science Foundation (Research Applied to National Needs), with partial support from the U.S. Environmental Protection Agency.

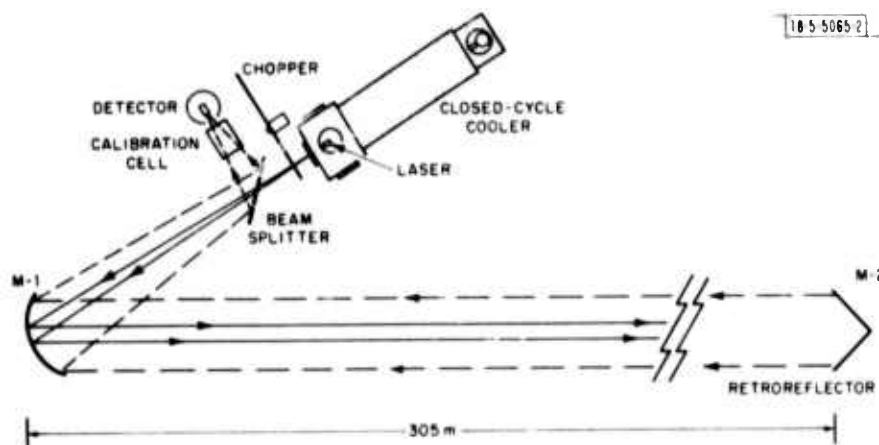


Fig. II-10. Schematic of long-path (305-m) diode laser and optical system for monitoring atmospheric carbon monoxide pollutant.

The most essential components of the tunable laser and optical systems are sketched in Fig. II-10. The $\text{PbS}_{0.845}\text{Se}_{0.185}$ laser was mounted inside a CTi closed-cycle cryogenic cooler, Model 21. The only requirement to operate the closed-cycle cooler is a standard 115- or 250-V electrical power line capable of 1 kW steady load. The cooler operates on the principle of expansion cooling, which is based on the adiabatic and reversible expansion of a gas in performing work on the external load. This expansion results in a reduction of the gas (helium) temperature due to a decrease in its internal energy by the amount of work done.

The vacuum requirement inside the laser chamber is moderate (10^{-3} to 10^{-4} Torr), and typical cool-down time from room temperature to 15 K is about 30 minutes. A coil of heater wire and a silicon temperature sensor were attached to the cold finger and connected to a temperature controller with proper feedback circuits, in order to raise the laser temperature above the minimum 15 K and to regulate it to within 1 mK. This additional degree of temperature control is in fact an extra laser wavelength tuning parameter which contributes to a wider tuning range as well as better laser mode selection.

The laser radiation was collimated by an off-axis, aluminum-coated parabolic mirror, M-1, 12 cm in diameter and transmitted across the 305-m path to a 12-cm corner-cube retroreflector, M-2, housed inside the other building. The return beam followed the same path, reflecting from the collimating mirror to a Ge beam splitter, finally impinging on the InSb (liquid N_2 -cooled) detector. Initial alignment of the infrared beam was usually assisted by a visible He-Ne laser beam.

Instead of applying the usual absorption technique by analyzing the amount of decrease in transmission, we employed the derivative spectroscopy method,^{1,2} which allowed for better electronic data processing to combat the problems of atmospheric turbulence and scattering over the long path. We found thermal effects in the atmosphere to be the main cause of the optical degradation of the received laser signal. Thermal gradients in the atmosphere caused beam defocusing and steering effects similar to those reported for other laser systems.¹² For example, we always found the best signal stability on a rainy day, when the ambient temperature variation over the path was small.

The derivative spectroscopy method involves taking the derivative of the absorption spectra. This was accomplished by modulating the diode current with a small (5 percent) superimposed sinusoidal current at a high frequency (~ 10 kHz). Since the laser emission frequency was modulated, the derivative of the absorption spectrum was obtained by synchronous detection at 10 kHz. At this high frequency, the effect of turbulence was minimized since the atmosphere was effectively "frozen" in this time scale. The chopper (170 Hz) in Fig. 11-10 provided the "direct" transmission and absorption signal, and current modulation at 10 kHz supplied the derivative signal due to CO. A typical set of these signals is shown in Fig. 11-11. Both in-house calibration and long-path signals are displayed in the figure for comparison. The calibrations were taken by optically short circuiting the laser radiation "in house" by an auxiliary small retroreflector. Figure 11-11(a) shows the absorption dips in the laser transmission signal and Fig. 11-11(b) is the corresponding derivative signals. The relative signal strength of the derivative peaks for the long-path case in part (b) of the figure is proportional to average concentrations of CO over 610 meters. The long-term fluctuation in the atmosphere was eliminated electronically by ratioing the derivative and transmitted signals, since both of them are usually affected in the same amount. Therefore, CO concentration is directly proportional to the ratioed signal and is independent of atmospheric fluctuations in the received laser power. Continuous data logging of the ratioed signal at the positive peak of the derivative scan in Fig. 11-11(b) on a strip-chart recorder provides the final system output of long-path CO pollutant monitoring.

A 10-cm calibration cell shown in Fig. 11-10 was necessary in order to obtain quantitatively the amount of CO in the long path. Since the path-length ratio of a 10-cm cell to a 610-meter-long path is 1/6100, a calibration gas of 100 ppm of CO in the cell corresponds to 16.4 ppb over the long path. The ambient CO concentration scale was established by comparing the extra

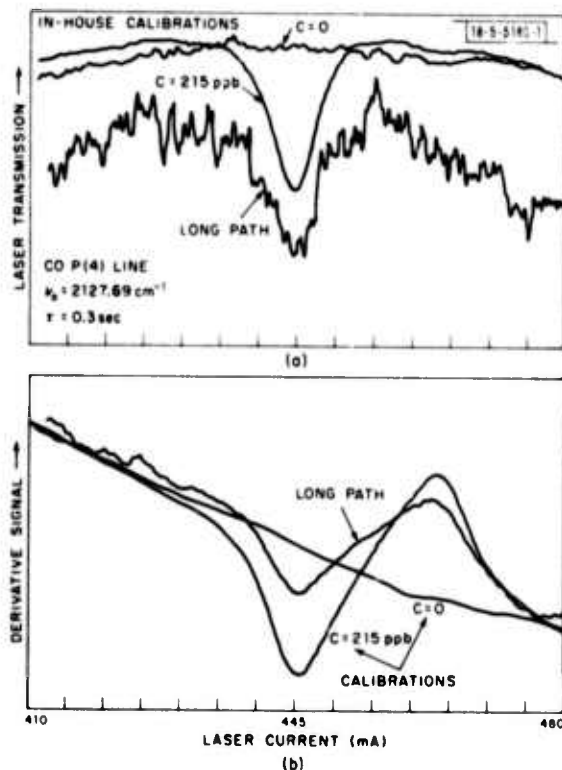


Fig. 11-11. (a) Laser transmitted signal for both in-house calibrations and ambient path detected synchronously at chopper frequency of 170 Hz. (b) Derivative signals corresponding to (a) detected at AC modulation frequency of 10 kHz. Line center of the derivative signal shift to 447 mA from 445 mA in (a) is the result of additional heat from AC modulation current.

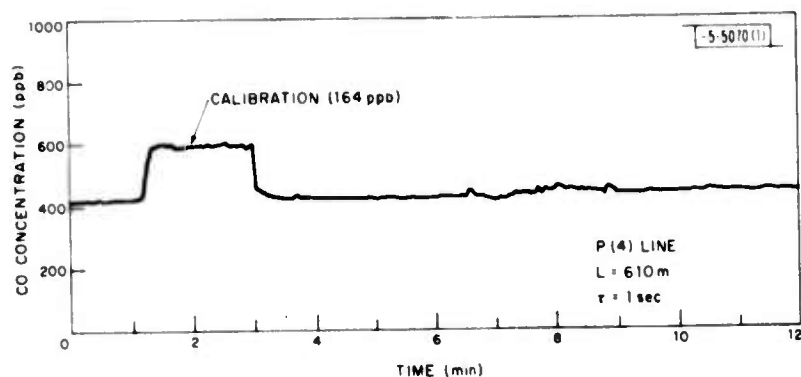


Fig. II-12. Continuous laser monitoring of ambient CO levels over the long path (610-m) on a strip-chart recorder with 1-sec integration time.

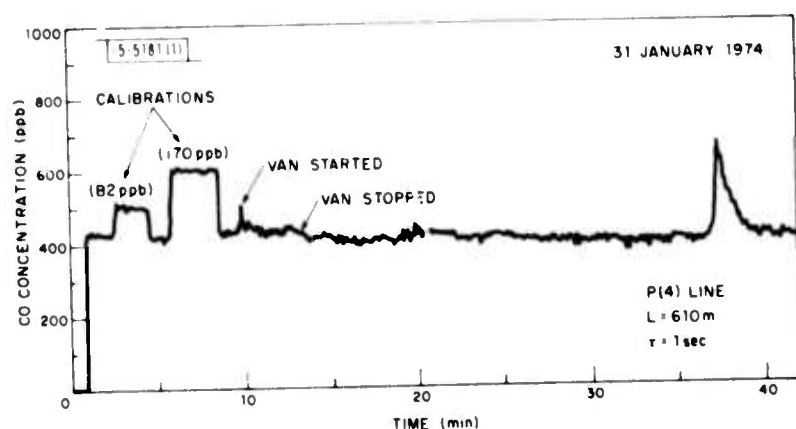


Fig. II-13. Continuous long-path (610-m) laser monitoring of ambient CO levels on a strip-chart recorder with 1-sec integration time.

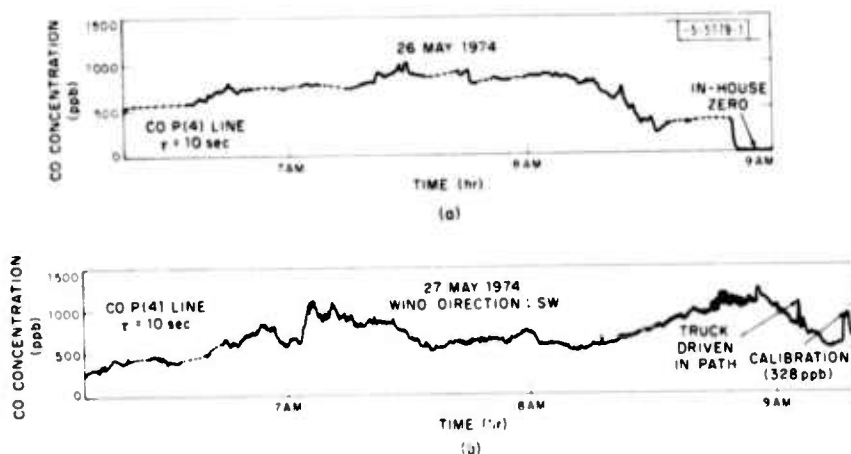


Fig. II-14. Unattended long-path (610-m) laser monitoring of ambient CO levels for several hours around 8:00 a.m. on two successive mornings showing the effects of rush-hour traffic.

deflection in the ratio signal due to calibration gases in a 10-cm cell. System linearity can be checked by using several concentrations of calibration gases.

The most sensitive CO monitoring over the 610-m path is shown in Fig. II-12 which represents a 12-min. run of the ratioed signal using the P(4) line. The peak-to-peak noise in the order of integration time is no more than the width of the recording pen, which shows an upper limit of ± 2.5 ppb of CO minimum detectable signal in this case. Since the value of the minimum detectable signal represents the system noise level, it also had to be checked by tuning the laser off the resonance line, i.e., adjusting the DC laser current to be on the wing instead of peak in the derivative scan shown in Fig. II-11(b). The off-line minimum detectable signal was also verified to be less than the width of the recording pen (~ 2.5 ppb). The 164-ppb calibration trace between 1 and 3 minutes was obtained by admitting premixed CO and air into the 10-cm cell (see Fig. II-10). The scale for the ambient CO concentration was therefore established. The slight increase in the ambient CO level between 6 and 9 minutes is the result of driving an automobile deliberately along the path to generate more CO for detection.

Measurements of longer durations have also been carried out. Figure II-13 is a similar monitoring result taken on a different day. The two calibration levels at the beginning of these traces were for 500 and 1050 ppm in a 10-cm cell equivalent to 82 and 170 ppb in the long path. A laboratory motor vehicle was intentionally started at approximately 10 minutes near the path; the CO level monitored correspondingly increased sharply. From the results between 10 and 14 minutes, we observed that the CO pollution emitted by the car caused a 10 percent rise in the ambient level after the initial spike. It can be reasoned that when the car first started, its exhaust contained large amounts of CO due to the rich gas mixture for a cold engine. When the engine was warmed up and running smoothly, the combustion was more efficient, which then reduced the CO pollutants in the exhaust. The source for a large increase in CO concentration at 39 minutes could not be identified, even though one could speculate that the parking lot or the nearby airport might be the guilty polluter.

Several measurements were performed essentially unattended for several days. The only problem was that a large amount of beam misalignment occurred with temperature deviation at different times of the day. However, we have some good continuous 3- to 4-hour data to illustrate the system ability for unattended CO monitoring. Figure II-14(a) and (b) was taken in the early morning on successive days. Notice a general increase in the CO levels as traffic picked up toward 8:00 a.m. in the rush-hour period. Since the path is only a few miles northwest of the superhighway, Route 128, it is therefore not surprising to see that kind of change in ambient CO levels before and after the rush hours with proper wind directions. Similarly, Fig. II-15 shows the variation in average CO concentration around 5:00 p.m. rush hours on a different day, along with the laser transmission signal. CO concentrations in the path seemed to increase and vary suddenly for this case, probably due to meteorological factors such as wind direction and speed. The detailed correlation of the time-varied CO levels and corresponding ambient conditions in a given area will be necessary to develop an applicable pollutant dispersion model for future predictions.

The major area for further work is to design a servo-controlled system to keep the mirror aligned with the retroreflector automatically. Depending upon the atmospheric thermal conditions, this will enable the system to make measurements unattended around the clock. Multi-pollutant monitoring should be extended from this kind of system by further modifications of the laser holder and optical arrangement. Our immediate plan calls for lasers to be fabricated

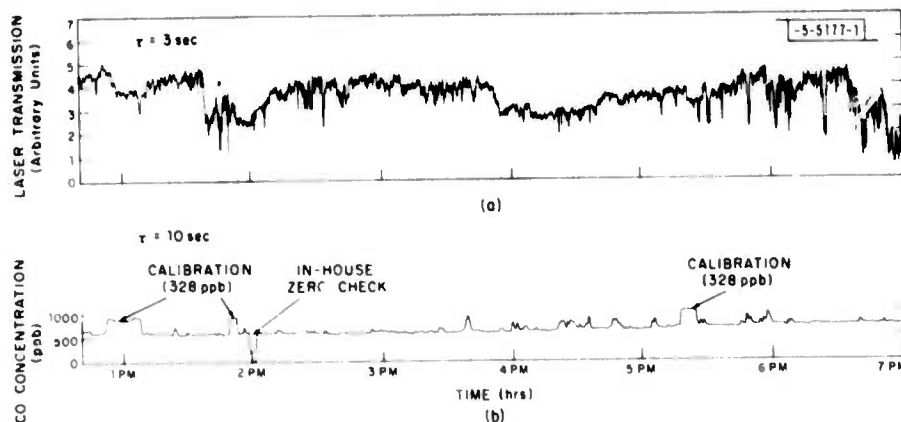


Fig. 11-15. Unattended long-path (610-m) laser monitoring for several hours around 5.00 p.m.; (a) Laser transmitted signal, (b) CO monitoring data.

in the 8.8- μm and 5.3- μm ranges to monitor ambient SO_2 and NO pollutants over a long path. In addition, a similar system is being assembled inside a motor van which will be driven to St. Louis to participate in the U.S. EPA Regional Air Pollution System programs in the summer of 1974. Pollution results from our system for CO will be checked against other newly developed sensitive CO point monitors. The area coverage of CO concentration results from our system and the point monitor's data should provide some of the required input parameters for computer modeling and predicting area pollution dispersions.

E. D. Hinkley
R. T. Ku
J. O. Sample

REFERENCES

1. Optics Research Report, Lincoln Laboratory, M.I.T. (1973:2), p. 59, DDC AD-779917.
2. D. Kelsall, J. O. S. A. 63, 1472 (1973).
3. A. R. Calawa, J. Luminescence 7, 477 (1973).
4. T. C. Harman, J. Phys. Chem. Solids Suppl. 32, 363 (1971).
5. R. A. McClatchey, Technical Report AFCRL-71-0370, Air Force Cambridge Research Laboratories (1 July 1971).
6. R. A. McClatchey and J. E. Selby, Technical Report AFCRL-72-0312, Air Force Cambridge Research Laboratories (23 May 1972).
7. E. D. Hinkley and P. L. Kelley, Science 171, 635 (1971).
8. E. D. Hinkley, J. Opto-Electronics 4, 67 (1972).
9. H. Kildal and R. L. Byer, Proc. IEEE 59, 1644 (1971).
10. Cryocooler Model 24, Cryogenic Technology, Inc., Waltham, Mass.
11. K. Westberg, N. Cohen and K. W. Wilson, Science 171, 1013 (1971).
12. E. R. Ochs and R. S. Lawrence, ESSA Technical Report ERL 106-WP16, Environmental Science Services Administration, Department of Commerce, Boulder, Colorado (February 1969).